ATLAS NOTE

ATLAS-CONF-2014-006

March 4, 2014

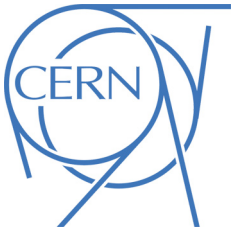

A general search for new phenomena with the ATLAS detector in pp collisions at $\sqrt{s} = 8$ TeV

The ATLAS Collaboration

Abstract

This note presents a model-independent general search for new phenomena in proton-proton collisions at a centre-of-mass energy of 8 TeV with the ATLAS detector at the LHC. The data set corresponds to a total integrated luminosity of 20.3 fb^{-1}. Event topologies involving isolated electrons, photons and muons, as well as jets, including those identified as originating from b-quarks (b-jets) and missing transverse momentum are investigated. The events are subdivided according to their final states into exclusive event classes. For the 697 classes with a Standard Model expectation greater than 0.1 events, a search algorithm tests the compatibility of data against the Monte Carlo simulated background in three kinematic variables sensitive to new physics effects. Although this search approach is less sensitive than optimized searches for specific models, it provides a more comprehensive investigation for new physics signals. No significant deviation is found in data. The number and size of the observed deviations follow the Standard Model expectation obtained from simulated pseudo-experiments.

ATLAS-CONF-2014-006
04 March 2014

1 Introduction

The LHC proton–proton collision data recorded by the ATLAS experiment have been thoroughly analyzed for specific signals of physics beyond the Standard Model (SM), and stringent limits have been set on new physics models. Although these searches cover a wide variety of possible event topologies, they are not exhaustive. Events produced by new interactions or new particles might still be hidden in the data. The analysis described in this note extends these specific searches with a model-independent approach. The search is designed to be comprehensive for new physics (NP) signals appearing at high transverse momenta (p_{T}). The approach is not sensitive to final states with low p_{T} particles or low cross-section signals overwhelmed by large contributions from SM background. This analysis is a continuation of a previous preliminary ATLAS search [1] at $\sqrt{s} = 7$ TeV which was based on 4.7 fb^{-1}of data collected in 2011. Model-independent searches have also been performed by the D0 [2], H1 [3,4], CDF [5] and CMS [6] experiments. The strategy presented here is based on the approach developed by the H1 experiment.

All event topologies involving electrons, photons, muons, jets, jets originating from b-hadrons (b-jets) and missing transverse momentum ($E_{\mathrm{T}}^{\mathrm{miss}}$) are investigated in a single analysis. Three kinematic distributions sensitive to contributions from NP are scanned for deviations from the SM prediction. A statistical search algorithm looks for the region of largest deviation between data and the SM, taking into account systematic uncertainties. The SM prediction is mainly constructed from Monte Carlo (MC) simulation. To quantify the compatibility of the data with the SM prediction, the distribution of the p-values of the observed deviations is compared to an expectation obtained from pseudo-experiments that includes statistical and systematic uncertainties and their correlations between search classes.

If a significant deviation is found, a dedicated analysis will be required to determine if the deviation is caused by a mismodeling of the SM prediction, or by a signal of new physics.

The data sample used in this analysis was recorded in 2012 at a centre-of-mass energy of 8 TeV. Application of beam, detector and data-quality requirements results in a data set with a total integrated luminosity of 20.3 fb^{-1}.

The note is organized as follows. Section 2 includes a description of the ATLAS detector. Section 3 describes the modeling of SM backgrounds, section 4 the event selection and section 5 the systematic uncertainties. The statistical scanning algorithm and the results are presented in section 6.

2 The ATLAS experiment

ATLAS [7] is a multipurpose particle physics detector with a cylindrical geometry and nearly 4π coverage in solid angle[1]. The inner tracking detector (ID) consists of a silicon pixel detector, a silicon microstrip detector, and a transition radiation tracker. The ID is surrounded by a thin superconducting solenoid providing a 2 T magnetic field. In the pseudorapidity region $|\eta| < 3.2$, high-granularity liquid-argon (LAr) electromagnetic (EM) sampling calorimeters surround the solenoid magnet. An iron-scintillator tile calorimeter provides coverage for hadronic particles over $|\eta| < 1.7$. The end-cap and forward regions, spanning $1.5 < |\eta| < 4.9$, are instrumented with LAr calorimetry for both EM and hadronic measurements. The muon spectrometer (MS) surrounds the calorimeters and consists of three large superconducting toroids, a system of precision tracking chambers, and detectors for triggering.

[1] ATLAS uses a right-handed coordinate system with its origin at the nominal interaction point in the centre of the detector and the z-axis along the beam pipe. Cylindrical coordinates (r, ϕ) are used in the transverse plane, ϕ being the azimuthal angle around the beam pipe. The pseudorapidity η is defined in terms of the polar angle θ by $\eta = -\ln\tan(\theta/2)$.

3 Monte Carlo samples

All processes producing high p_{T} objects with non negligible cross-section are considered for the SM estimate: inclusive jets production, $W/Z/\gamma$ production in association with jets, single top and top pair production including their association with jets and vector bosons, diboson, triboson and Higgs production. In addition, samples of new physics are considered as benchmark signals. Most MC samples are produced using a GEANT4 [8] based full detector simulation [9], while the top pair, W+jets, Z+jets, γ+jets and the SUSY signal samples are passed through a fast simulation using a parameterisation of the performance of the ATLAS electromagnetic and hadronic calorimeters [10] and a GEANT4 based simulation elsewhere. Several corrections are applied to the MC to reproduce the reconstruction efficiencies of muons, electrons and photons measured in data. Additional scale factors are used to correct the b-tagging reconstruction and misidentification efficiencies.

The simulation includes the effect of multiple pp interactions, denoted as pileup, and is weighted to reproduce the distribution of the average number of collisions per bunch crossing observed in data. Most of the MC samples used correspond to a total integrated luminosity much larger than that in data (typically from a few 100 to a few 1000 fb^{-1}). Samples of processes with high cross-section, such as multijet production with low p_{T} jets and the associated production of a vector boson and jets, with a low p_{T} vector boson, have a total integrated luminosity of the order of few fb^{-1}. The statistical uncertainty of the MC samples is taken into account in the search algorithm.

Multijet production
Simulated multijet events are generated with Pythia-8.165 [11], which uses $2 \to 2$ Leading-Order (LO) matrix elements (ME) with the AM2 parameter tune [12] and the `MSTW2008LO` [13] LO parton distribution function (PDF) set.

$Z/\gamma*$ and W+jet production
Samples of W and $Z/\gamma*$ in association with jets are simulated with the Sherpa-1.4.0 [14] MC generator with up to 5 extra partons in the matrix element. Both b- and c-quarks are treated as massive. The samples are normalized to the NNLO incusive cross-section calculation in Ref. [15]. PDFs are taken from the next-to-leading-order PDF set `CT10` [16].

γ+jets and $\gamma\gamma$+jets
Photon plus jets samples are generated with Sherpa-1.4.0 with up to 4 extra partons in the matrix element. Prompt diphoton samples are generated with Alpgen-2.14 and Pythia-6.426 [17] in various ranges of the invariant diphoton mass. These samples include the processes $gg \to \gamma\gamma$ and $q\bar{q} \to \gamma\gamma$. A filter is applied to only select events where the two photons have $p_{\mathrm{T}} > 35$ GeV.

W/Z+γ/$\gamma\gamma$
The $W\gamma$ samples are generated using Alpgen-2.14 [18] interfaced to Pythia-6.426. A generator level filter requiring at least one photon with $p_{\mathrm{T}} > 10$ GeV is applied. The $Z\gamma$ process is generated with Sherpa-1.4.0. The PDF set used for these samples is `CTEQ6L1` [19]. Sherpa-1.4.0 is also used to generate W/Z+$\gamma\gamma$ samples, with a leading-order matrix element. A k-factor of 1.2 is applied to the W/Z+γ samples, while we use a k-factor of 2 and 3 for $Z + \gamma\gamma$ and $W + \gamma\gamma$, respectively, based on the next-to-leading order (NLO) calculations [20, 21].

Top quark pair and single top production
The production of top quark pairs is simulated with Powheg-1.0 [22] interfaced to Pythia-6.426 (with the Perugia 2011C tune) for the fragmentation and the hadronization processes. The top-quark mass is fixed

to 172.5 GeV. The NLO PDF set CT10 is used. The $t\bar{t}$ cross-section has been calculated at NNLO in QCD including resummation of next-to-next-to-leading logarithmic (NNLL) soft gluon terms with Top++2.0 [23–28]. Single top samples for the Wt and s-channels are generated with Powheg-1.0 + Pythia-6.426 (Perugia 2011C tune) and the PDF set CT10. The single top sample for the t-channel production is generated with AcerMC-3.8 and Pythia-6.426 and the PDF set CTEQ6L1. They are normalized to the NLL calculations in Refs. [29–31]. An additional sample generated with MadGraph-5.1.4.8 + Pythia-8.165 and the MSTW2008LO PDF is used for SM production of four top quarks.

Top and vector boson associated production
Top quark pair production also occurs with an additional electroweak boson (W, $Z/\gamma*$) or a real photon. These samples are simulated with MadGraph-5.1.4.8 interfaced to Pythia-6.426 including up to two extra partons. An additional sample is generated with MadGraph-5.1.4.8 + Pythia-8.165 and the MSTW2008LO PDF set for exclusive $t\bar{t}WW$ production. Samples for single top production in association with a leptonically decaying Z boson, generated with MadGraph-5.1.4.8 interfaced to Pythia-6.426 and the CTEQ6L1 PDF, have also been included. Samples of $t\bar{t}$ + W and $t\bar{t}$ + Z are normalized to the NLO cross-section calculated in [32, 33], the others to the LO cross-section from the generator.

Massive diboson production
Diboson (WW, WZ and ZZ) events are simulated using Powheg-1.0+Pythia-6.426 and the PDF set CT10. In these samples leptonic decays are enforced. No filter is applied for WW while for WZ and ZZ a filter is applied to select events with a generator level mass of the off-shell Z larger than 4 GeV and two leptons with $p_{\mathrm{T}} > 5$ GeV. Separate samples generated with Sherpa-1.4.0 are used to include the case in which a boson decays to hadrons. They are normalized to NLO inclusive cross-sections obtained with MCFM [34]. Due to much larger W/Z+jets and multijet cross-sections, the contribution from hadronic diboson decays is negligible.

Massive triboson production
The triboson processes WWW, ZWW and ZZZ are generated with MadGraph-5.1.4.8 +Pythia-6.426 at LO for the case in which all bosons decay leptonically, while Sherpa-1.4.0 is used for the case where one of the bosons decays into hadrons. They are normalized to the NLO inclusive calculation described in Ref. [35].

Higgs production
SM Higgs production (with a mass of 125 GeV) is also included as a background. Samples are generated using either Pythia-8.165 with CTEQ6L1 PDF set or with Powheg-1.0+Pythia-8.165 and the CT10 PDF. The samples are normalized to the cross-sections recommended by the LHC Higgs cross-section working group [36].

New physics signal samples
The production of supersymmetric [37–45] particles is considered as a first benchmark signal of new physics. Since this analysis searches for large deviations, the sensitivity of the search needs to be compared to the discovery sensitivity and not the exclusion sensitivity.

One set of signals is the pair production of top squarks (stop) $\tilde{t}$ with the decay $\tilde{t} \to t\tilde{\chi}_1^0$. The $\tilde{t}$ masses considered are 400, 500 or 600 GeV, with a stable massless neutralino $\tilde{\chi}_1^0$. The second set of benchmark signals considers the pair production of gluinos which decay through a virtual stop of mass 2.5 TeV to $t\bar{t}\tilde{\chi}_1^0$ with a branching fraction of 100%. Here the mass of the neutralino is set to 100 GeV and gluino masses of 800, 1000 and 1200 GeV are considered. Benchmark signals are generated with Herwig++

2.5.2 [46] and the CTEQ6L1 PDF set. Signal cross-sections are calculated to next-to-leading order in the strong coupling constant, adding the resummation of soft gluon emission at next-to-leading-logarithmic accuracy (NLO+NLL) [47–51].

A third set of benchmark signals is the production of a heavy Z' in the sequential SM, which assumes the same coupling to fermions as the SM Z boson [52]. The Z' masses considered are 1500, 2000 or 2500 GeV and the decays considered are to pairs of electrons or muons of opposite charge. The samples are generated with Pythia-8.165 and the MSTW2008LO PDF set.

4 Event selection, classification and background prediction

Events selected by the trigger are first subject to event cleaning and overlap removal requirements, using a baseline definition of physics objects. Tighter selections are used on the objects defining the event classes.

4.1 Object definition

Jet candidates are reconstructed using the anti-k_t jet clustering algorithm [53, 54] with a distance parameter of 0.4. The algorithm takes as inputs topological clusters, calibrated using local cluster weighting to account for the effects of non-compensation, dead material and out-of-cluster deposits [55, 56]. Jet momenta are constructed by performing a four-vector sum from these clusters, treating each as an $(E, \vec{p})$ four-vector with zero mass. These jets are corrected for the effects of calorimeter non-compensation and inhomogeneities by using p_{T}- and η-dependent calibration factors based on MC corrections validated with extensive test-beam and collision-data studies [57]. The dependence of the jet response on pileup conditions is significantly reduced by implementing a correction based on the "Jet-area method" [58, 59]. Except during the $E_{\mathrm{T}}^{\mathrm{miss}}$ computation, where the η range is not restricted, only jet candidates with $p_{\mathrm{T}} > 20$ GeV and $|\eta| < 2.8$ are subsequently retained.

Jets arising from b-quarks are identified within $|\eta| < 2.5$ by using information about track impact parameters and reconstructed secondary vertices [60]; the b-tagging algorithm is based on a neural network using the output weights of various b-tagging algorithms as input. An operating point is chosen such that 70% of truth b-jets and about 1% of light-flavour or gluon jets are selected in simulated $t\bar{t}$ events [61]. Charm-quark initiated jets are tagged with an efficiency of about 20%.

Electron candidates are required to have $p_{\mathrm{T}} > 10$ GeV, $|\eta| < 2.47$, to pass the 'medium' electron shower shape and track selection criteria of Ref. [62], and to be outside problematic regions of the calorimeter. Muon candidates are reconstructed by combining tracks in the ID and MS. Muons are required to have $p_{\mathrm{T}} > 10$ GeV and $|\eta| < 2.4$. Photon candidates are required to pass tight identification criteria [63], to lie in the fiducial region $|\eta| < 1.37$ or $1.52 < |\eta| < 2.37$ and to have $p_{\mathrm{T}} > 25$ GeV.

Following the steps above, overlaps between candidate jets with $|\eta| < 2.5$, leptons and photons are resolved using a method similar to Ref. [64]. First, any such jet candidate lying within a distance $\Delta R = \sqrt{(\Delta\eta)^2 + (\Delta\phi)^2} = 0.2$ from an electron or photon is discarded. Then any lepton or photon candidate remaining within a distance $\Delta R = 0.4$ of a jet candidate is discarded. Electrons within a distance of $\Delta R = 0.1$ to muons are removed.

Further selections are applied to the final objects used for classification. For electrons we require the transverse impact parameter significance of the track $d_0/\sigma(d_0)$, calculated with respect to the primary vertex (defined in Section 4.2), to be less than 5 and the longitudinal impact parameter $z_0 \sin\theta$ to be less than 0.4 mm.

The track-based isolation is defined as the scalar sum of the p_{T} of tracks inside a cone of $\Delta R < 0.3$ around the lepton track and should be smaller than $0.16 \cdot \min(p_{\mathrm{T}}, 60\ \mathrm{GeV})$. The tracks considered in the sum must be compatible with the lepton vertex and have $p_{\mathrm{T}} > 0.4$ GeV. The calorimeter-based isolation

uses the transverse energy deposited in the calorimeter in a cone of radius $\Delta R < 0.3$ around the lepton, corrected for the effect of pileup, and must be less than $0.18 \cdot \min(p_{\mathrm{T}}, 60\ \mathrm{GeV})$. Corrections for leakage of the electron energy in the isolation cone are also applied.

For muons the transverse impact parameter significance is required to be less than 3 and the longitudinal impact parameter less than 0.4 mm. Track and calorimetric isolation are required to be less than $0.12 \cdot \min(p_{\mathrm{T}}, 60\ \mathrm{GeV})$.

An isolation requirement is also applied to photons; photon candidates are removed if more than 4 GeV of transverse energy is observed in a cone of $\Delta R < 0.4$ surrounding the photon deposition in the calorimeter. The isolation energy is corrected for lateral leakage in the calorimeter, as well as for the average ambient energy in the event.

The measurement of the missing transverse momentum two-vector $\vec{p}_{\mathrm{T}}^{\,\mathrm{miss}}$ (and its magnitude $E_{\mathrm{T}}^{\mathrm{miss}}$) is based on the p_{T} of all jet and lepton candidates and all calorimeter clusters not associated to such objects [65]. Clusters associated to leptons or photons with $p_{\mathrm{T}} > 10$ GeV and those associated with jets with $p_{\mathrm{T}} > 20$ GeV make use of the calibrations of the respective objects. Clusters not associated with these objects are calibrated using both calorimeter and tracking information.

Thereafter, the remaining lepton and jet candidates are considered "reconstructed", and the term "candidate" is dropped. The same object identification and selection criteria are applied to data and MC events.

4.2 Event selection and trigger criteria

Events are selected using several triggers: single lepton and photon, single or multijet and $E_{\mathrm{T}}^{\mathrm{miss}}$. These triggers reach their maximal efficiencies after applying the offline selection listed in Table 1.

In order to avoid double counting, events are taken from the different triggers according to the following priority order. Events with $E_{\mathrm{T}}^{\mathrm{miss}} > 150$ GeV are required to pass the $E_{\mathrm{T}}^{\mathrm{miss}}$ trigger. Events failing this $E_{\mathrm{T}}^{\mathrm{miss}}$ requirement but with a muon with $p_{\mathrm{T}} > 25$ GeV are required to pass the muon trigger. Remaining events with electrons with $p_{\mathrm{T}} > 25$ GeV or photons with $p_{\mathrm{T}} > 40$ GeV are taken from electron and photon triggers. Events containing a jet (or b-jet) with $p_{\mathrm{T}} > 500$ GeV or 5 jets (or b-jets) with $p_{\mathrm{T}} > 80$ GeV are required to pass the jet and multijet triggers respectively.

Following the object reconstruction described above, events are discarded if they have any jets failing quality selection criteria designed to suppress detector noise and non-collision backgrounds [55]. Events are also required to have a primary vertex reconstructed from five or more tracks with $p_{\mathrm{T}} > 0.4$ GeV; the vertex with the largest $\sum p_{\mathrm{T}}^2$ of the associated tracks is chosen. Non-collision backgrounds were studied in several ATLAS analyses with identical object selection criteria and these backgrounds were found to give a negligible contribution after applying event cleaning selections [66].

Trigger	Offline Selection
muon:	$p_{\mathrm{T}} > 25$ GeV
electron:	$p_{\mathrm{T}} > 25$ GeV
photon:	$p_{\mathrm{T}} > 140$ GeV
$E_{\mathrm{T}}^{\mathrm{miss}}$:	$E_{\mathrm{T}}^{\mathrm{miss}} > 150$ GeV
single jet:	$p_{\mathrm{T}} > 500$ GeV
multijet:	$p_{\mathrm{T}}(jet_{1,\cdots,5}) > 80$ GeV

Table 1: Requirements on individual physics objects applied at the offline reconstruction level to obtain maximum trigger efficiency.

4.3 Event classification

The events are subdivided into exclusive classes based on the number and types of objects reconstructed in the event; electrons (e), muons (μ), photons (γ), jets (j), b-jets (b) and $E_{\mathrm{T}}^{\mathrm{miss}}$ (ν) are considered. We choose not to use taus or lepton charge information for the classification. The subdivision can be regarded as a classification according to the most important features of the events. The p_{T} cuts applied on top of the trigger selection and the labels used for each object are summarized in Table 2.

The classification includes all possible final state configurations and object multiplicities, e.g. if a data event with 7 reconstructed muons is found it is classified in a "7-muon" event class (7μ). Similarly an event with missing transverse momentum, 2 muons, 1 photon and 4 jets is classified and considered in a corresponding event class denoted ($\nu 2\mu 1\gamma 4j$).

To suppress sources of fake $E_{\mathrm{T}}^{\mathrm{miss}}$ two additional requirements are applied on events to be classified in ν categories. The ratio of $E_{\mathrm{T}}^{\mathrm{miss}}$ over m_{eff} (where m_{eff} is defined in each event class as the scalar sum of the p_{T} of the objects defining the class, including the $E_{\mathrm{T}}^{\mathrm{miss}}$) is required to be greater than 0.2 and the minimum azimuthal separation between the $E_{\mathrm{T}}^{\mathrm{miss}}$ and the three leading reconstructed jets (if present) has to be greater than 0.4, otherwise the event is rejected.

Some final states covered in this search have blinded signal regions in dedicated new physics searches and they are therefore excluded from this search. These final states are monojet and monophoton, final states with four or more b-jets and final states with one electron or one muon and additional $E_{\mathrm{T}}^{\mathrm{miss}}$. Final states with 2 photons without additional leptons and without $E_{\mathrm{T}}^{\mathrm{miss}}$ are not expected to be well modelled by the MC prediction due to the large multijet background and have been excluded from the analysis. Multijet background is expected to be negligible for final states with 2 photons and additional leptons or $E_{\mathrm{T}}^{\mathrm{miss}}$.

Object	jet	b-jet	electron	muon	photon	$E_{\mathrm{T}}^{\mathrm{miss}}$
Label	j	b	e	μ	γ	ν
Lower p_{T} cut	50 GeV	50 GeV	25 GeV	25 GeV	40 GeV	150 GeV

Table 2: List of objects used for the event classification with their label and lower p_{T} requirement.

4.4 Background estimation

In this search the SM prediction for almost all processes is taken from MC simulation. Only background events with one lepton candidate originating from misidentification of hadronic jets, photon conversions or real leptons from heavy flavor decays (collectively referred to as fake leptons) are estimated using data. For categories containing more than one lepton the contribution from fake leptons is found to be small compared to the total background and taken directly from the simulation. Comparisons between data and simulation in dedicated control regions with enlarged fake-lepton contribution have shown agreement within uncertainties. Re-weighting procedures are applied to some of the MC samples to improve the modeling of the SM background. This is described in section 4.4.2.

4.4.1 Estimation of fake lepton background

Background contributions with exactly one fake lepton are determined with a data-driven procedure referred to as the ABCD method.

In an ABCD method the background rate is estimated by applying the event selections on two independent, uncorrelated variables, such that both selections enhance the signal to background ratio. This

separates the phase-space into four regions: a signal dominated and three background enhanced regions.

The two variables used here are the relative track isolation of the lepton and the track impact parameter significance, in which the requirements applied for signal leptons (Section 4.1) are reverted. The expected number of background events in the signal dominated region A can be determined from the observed data events in the other three regions as $N_A = N_C \times N_B/N_D$, after removing the prompt leptons contribution predicted by the MC in regions B, C and D. The method has been tested on MC samples, and from the accuracy of the results an uncertainty of 50% is assigned to the fake lepton estimate for all event classes. The method is validated with data at low transverse and low effective mass in 1 lepton classes with 1 jet, 3 jets, and 1 jet and 1 b-jet. By applying this data-driven procedure the analysis has reduced sensitivity to NP models predicting non-isolated leptons.

4.4.2 Corrections to the MC prediction

In classes containing only j and b the multijet MC samples are scaled to data with normalization factors, ranging from 0.4 to 1, derived separately in each exclusive jet multiplicity class (e.g. for the $1j2b$ the same normalization factor as for the $3j$ category is used). After this scaling is applied we lose sensitivity to NP effects causing only normalization differences between data and the MC prediction in event classes containing only j and b.

The simulated W/Z+jets and top pair samples are reweighed to improve the modeling in classes containing ν, by reweighing the truth-level p_{T} distribution of the boson or top quark pair. The W/Z+jets correction was determined in a control region requiring one lepton and high $E_{\mathrm{T}}^{\mathrm{miss}}$ by the search for stop decays to charm and neutralinos [67]. The correction of the $t\bar{t}$ p_{T} distribution was determined in a search for squarks and gluinos in decays with one isolated lepton and derived in a control region requiring one lepton, high $E_{\mathrm{T}}^{\mathrm{miss}}$, 3 or 5 jets and one b-tagged jet [68]. These corrections lead to a lower SM prediction for classes with $E_{\mathrm{T}}^{\mathrm{miss}}$. The reweighing has no effect on the largest positive deviations, but decreases the number of deficits seen in data.

5 Systematic uncertainties

The systematic uncertainties have both uncorrelated components and components which are correlated between event classes and within different bins of kinematic distributions in the same event class. The correlated component is taken as a normalization uncertainty assigned coherently to all bins and event classes. The uncorrelated components vary independently among different bins and event classes. In the search algorithm, all uncertainties are treated as uncorrelated. Correlations according to the correlated uncertainty components are, however, used for the generation of the pseudo-experiments. The experimental uncertainties and the uncertainty due to the limited number of MC events are found to dominate in the majority of the event classes.

5.1 Experimental uncertainties

The dominant detector-related systematic effects are due to the uncertainties in the jet energy scale (JES) and resolution (JER), and due to the limited knowledge of the b-tagging efficiencies. The JES uncertainty estimate is based on MC studies, test-beam data and in-situ measurements [55,69,70]. Additional uncertainties account for jet-flavour and pileup-dependent effects. Uncertainties in the JER are obtained from in-situ measurements of the jet response asymmetry in di-jet events [71]. Jet uncertainties are propagated to the measurement of the $E_{\mathrm{T}}^{\mathrm{miss}}$, and additional uncertainties arising from energy deposits not associated with any cluster are also included. The uncertainty on the b-tagging efficiency is derived from samples of muons associated with jets and $t\bar{t}$ events [61,72]. The mis-tag probability for c and light jets is measured in inclusive jet samples [73].

The uncertainty on the electromagnetic (photon and electron) energy scales includes the effect of the uncertainty from the $Z \to ee$ control sample used to extract the scale factors, of the limited knowledge of the material, of the presampler energy scale and an additional uncertainty for low-p_{T} objects.

The resolution uncertainty of electromagnetic objects is estimated varying the corrections, determined in a sample of $Z \to ee$, to the resolution of the electromagnetic particle response in the simulation within their uncertainties.

An uncertainty on the photon ID efficiency is obtained from a comparison between data-driven measurements and simulated efficiencies in control samples [74].

Uncertainties on electron and muon reconstruction and identification efficiencies, as well as muon momentum scale and resolution, are not considered as they have been found negligible in all of the considered event classes.

A systematic uncertainty related to the pileup modeling is determined by comparing the nominal reweighting with a shift in the weight scale of 10%. The uncertainty on the integrated luminosity is 2.8%, derived by following the same methodology as that detailed in Ref. [75].

Experimental uncertainties are treated as correlated and the uncertainty due to the limited number of MC events is treated as uncorrelated in the pseudo-experiment generation.

5.2 Theoretical uncertainties

The principle of this analysis is to search for a deviation from the MC description and, if such a deviation is found, to study it with a dedicated analysis. Therefore no rigorous determination of the theoretical uncertainties was performed for the present general search.

Systematic uncertainties are assigned to represent typical theoretical uncertainties of the models and generators used. The uncertainties are motivated by theoretical studies and the results of dedicated searches and measurements by the ATLAS Collaboration at high p_{T}. All theory uncertainties are treated as constant over the studied parameter space. They are summarised for the SM processes considered in Table 3 and discussed below.

Theoretical uncertainties are assigned per subprocess and subdivided into an uncorrelated and a correlated component.

Multijet processes are modeled using MC samples for the $2 \to 2$ process only. However, since the jet multiplicity is reweighted to data, no cross-section uncertainty is applied. An uncorrelated uncertainty of 30% is assumed, based on studies described in Ref. [76], to cover any residual difference between data and Pythia-8.165.

Systematic uncertainties of 10% correlated and 30% uncorrelated are applied to γ+jets and $\gamma\gamma$+jets production processes. These values are a bit larger then the uncertainties quoted in Ref. [63].

The inclusive W/Z cross-sections are known at NNLO, with an uncertainty of $\approx 5\%$. We assign this 5% as a correlated uncertainty, while 15% is taken as uncorrelated uncertainty. These uncertainties are inspired by Ref. [77]. For W/Z+heavy flavour processes a correlated uncertainty of 30% is assigned and an uncorrelated uncertainty of 10%. The uncertainty for these processes is increased to be consistent with the reweighting and uncertainties found in other ATLAS analyses, e.g. in Ref. [68].

For $t\bar{t}$ and single top, for which the inclusive cross-section is known to NNLO and NLO, respectively, a correlated uncertainty of 5% and an uncorrelated uncertainty of 20% is used. We use slighly larger uncertainties than those given in Ref. [78].

For $t\bar{t}$ production with additional vector bosons we assign a 10% correlated uncertainty and a 30% uncorrelated uncertainty. Again these numbers are slighly more conservative than those determined from pure PDF and scale variation (see e.g. Refs. [32, 33]).

Diboson processes (including W/Z+γ) are known to NLO. A correlated uncertainty of 10% and an uncorrelated uncertainty of 30% are assigned for these processes. To cover possible shape uncertainties in specific phase-space regions and due to additional jet production we have quoted a more conservative

uncertainty than that in Ref. [79]. For triboson production (including W/Z+$\gamma\gamma$) we quote a correlated uncertainty of 20% and 50% as an uncorrelated uncertainty. Similar numbers are found in Ref. [80]. The same conservative uncertainties are used for the single top+Z and four top production. An uncorrelated uncertainty of 20% is used for all Higgs production processes to cover systematics in specific phase-space regions, e.g. with additional jet production. The correlated uncertainty is set to 5% due to the well-known Higgs cross-sections [36].

Process	correlated uncertainty (%)	uncorrelated uncertainty (%)
Multijet (normalized to data)	0	30
γ+jets and $\gamma\gamma$+jets	10	30
W/Z + jets production	5	15
W/Z + heavy flavour production	10	30
$t\bar{t}$ and single top	5	20
$t\bar{t}$ + vector boson	10	30
Diboson processes (including W/Z+γ)	10	30
Triboson	20	50
Higgs production	5	20

Table 3: Theoretical uncertainties assigned to the modelling of the background processes, subdivided into correlated and uncorrelated effects for the generation of the pseudo-experiments.

6 Results

6.1 Event yields

Data events are found in 573 event classes. The number of classes with an SM expectation larger than 0.1 is 697. These classes are further considered for the statistical analysis. A total of 16 event classes[2] have an SM expectation of less than 0.1 events, but at least one data event; two data events are found only in the $2\mu 1e5j$ event class. The data and MC prediction for the 697 classes with an SM expectation > 0.1 are shown in Figures 1 and 2 for event classes collected with the electron and photon triggers, in Figures 3, 4 and 5 with the muon trigger and in Figures 6, 7 and 8 with jets and $E_{\mathrm{T}}^{\mathrm{miss}}$ triggers. Agreement between data and the SM prediction is observed for most event classes.

6.2 Search algorithm

To quantify the level of agreement between the data and the SM expectation and to identify regions of deviations, we use a search algorithm first developed for the H1 generic search [3]. The algorithm has been applied to the m_{eff} (the scalar sum of the p_{T} of the objects defining the class, including the $E_{\mathrm{T}}^{\mathrm{miss}}$), the visible invariant mass and the $E_{\mathrm{T}}^{\mathrm{miss}}$ distributions. The visible invariant mass (m_{inv}) is defined for each event class as the invariant mass calculated with all objects defining the class besides the $E_{\mathrm{T}}^{\mathrm{miss}}$. The m_{eff} variable has been widely used in the context of searches for new physics, as it is sensitive to a large

[2]The 16 classes are: $3j2b$, $1\mu 1e6j2b$, $2\mu 1e5j$, $2\mu 8j$, $1\mu 1e2\gamma$, $1\mu 9j2b$, $4\mu 1j1b$, $2\mu 2e2j1b$, $1\mu 3e2j1b$, $3e2j3b$, $3e4j2b$, $\nu 2e1\gamma 2b$, $\nu 1e1\gamma 5j1b$, $\nu 2\mu 1e1j2b$, $15j$, $\nu 3e2b$

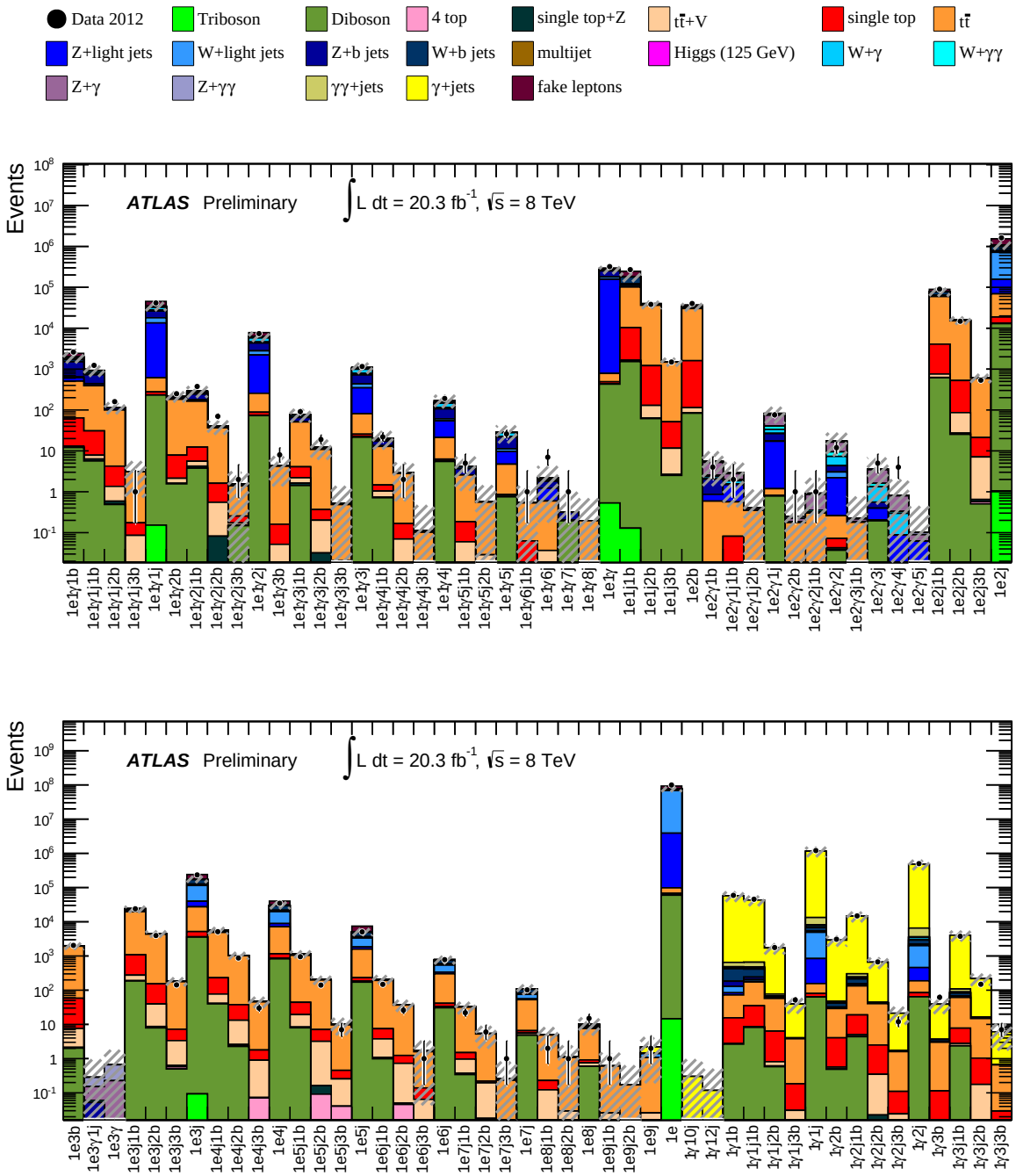

Figure 1: Number of events for event classes for which electron and photon triggers are used. The classes are labeled according to the abundance and type ($e, \mu, \gamma, j, b, \nu$) of the reconstructed objects for this event class. The data are compared to the SM background expectation as described in the text. The hatched bands indicate the total uncertainty of the SM prediction.

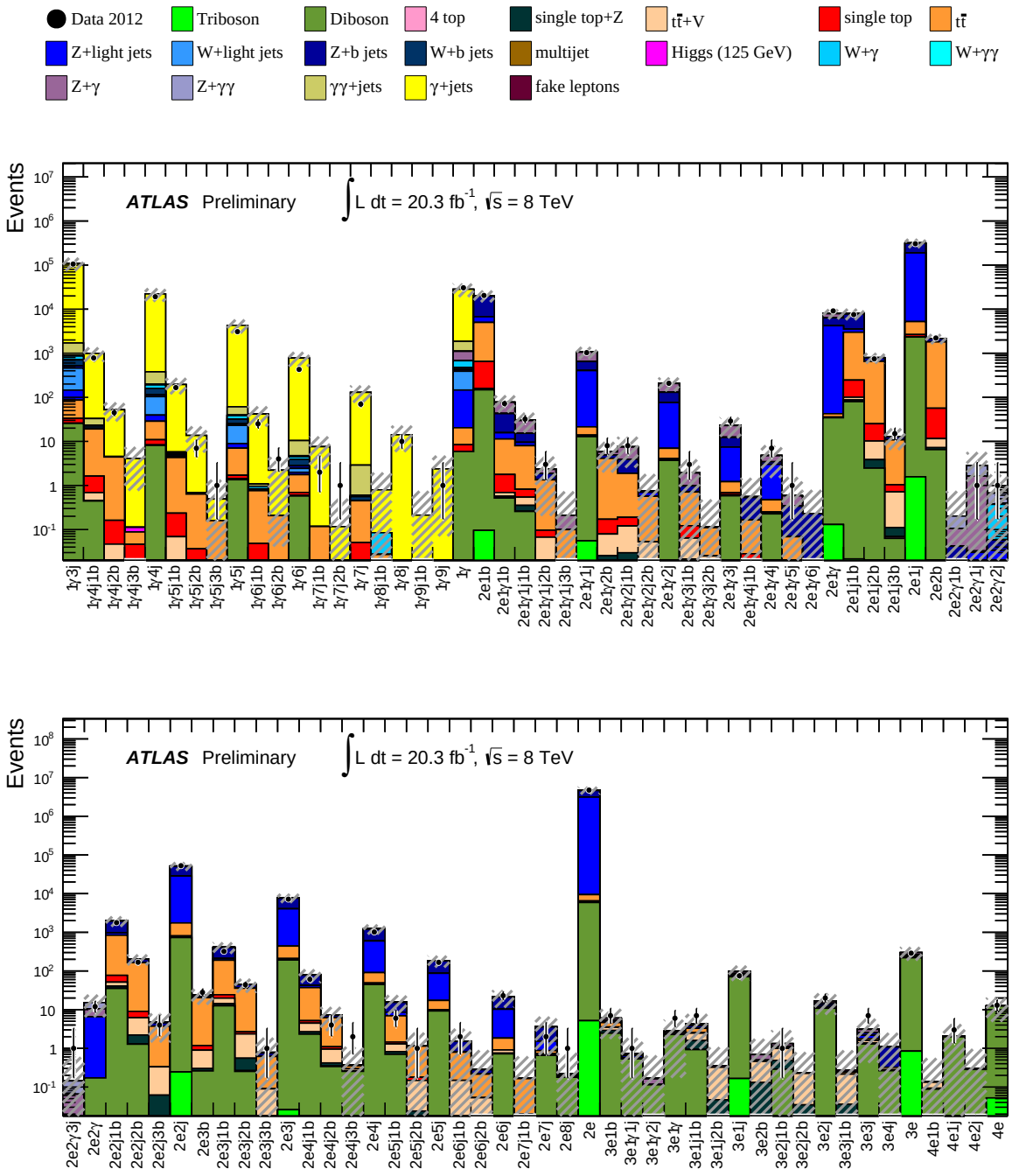

Figure 2: Number of events for event classes for which electron and photon triggers are used. The classes are labeled according to the abundance and type ($e, \mu, \gamma, j, b, \nu$) of the reconstructed objects for this event class. The data are compared to the SM background expectation as described in the text. The hatched bands indicate the total uncertainty of the SM prediction.

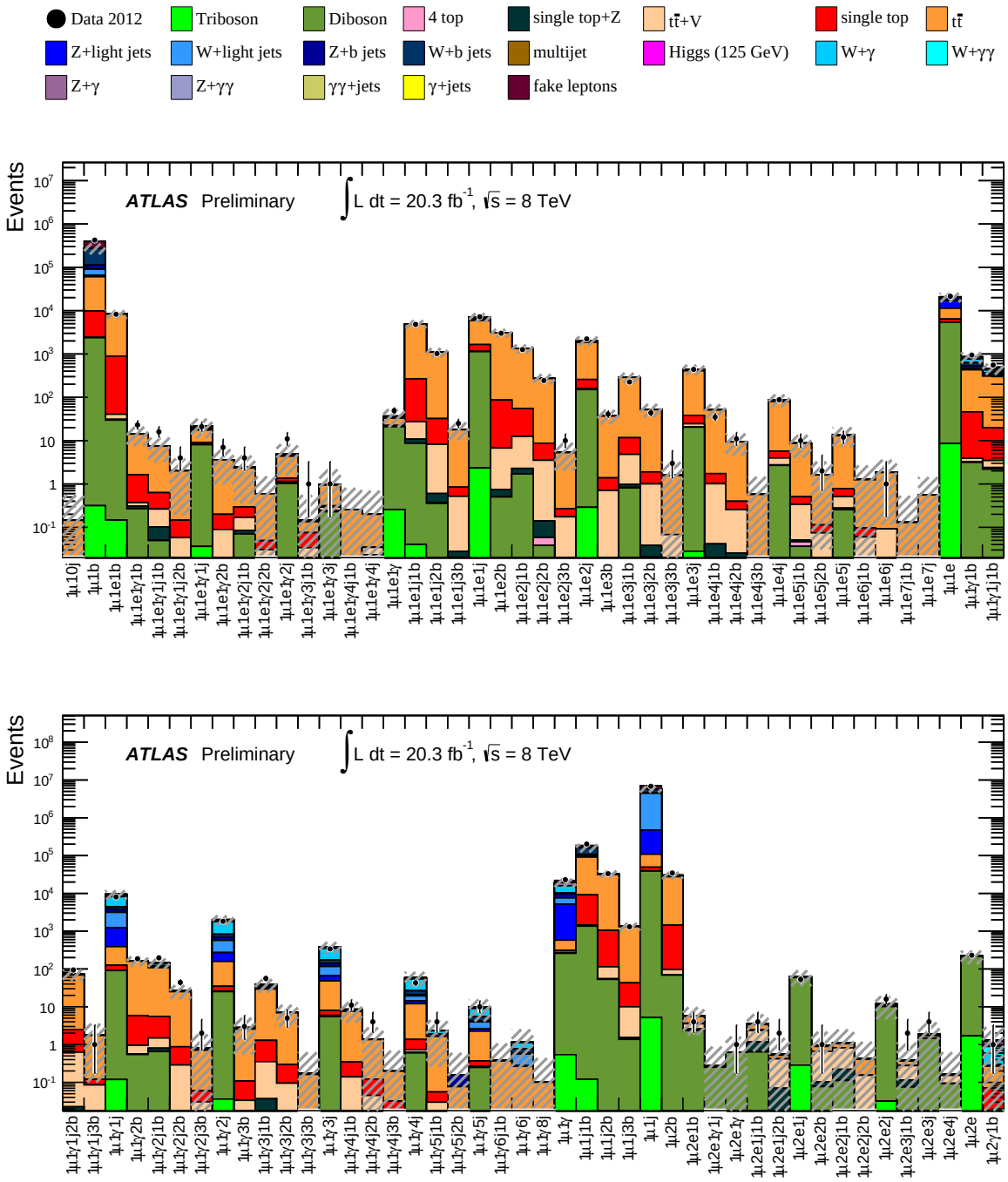

Figure 3: Number of events for event classes for which muon triggers are used. The classes are labeled according to the abundance and type (e, μ, γ, j, b, ν) of the reconstructed objects for this event class. The data are compared to the SM background expectation as described in the text. The hatched bands indicate the total uncertainty of the SM prediction.

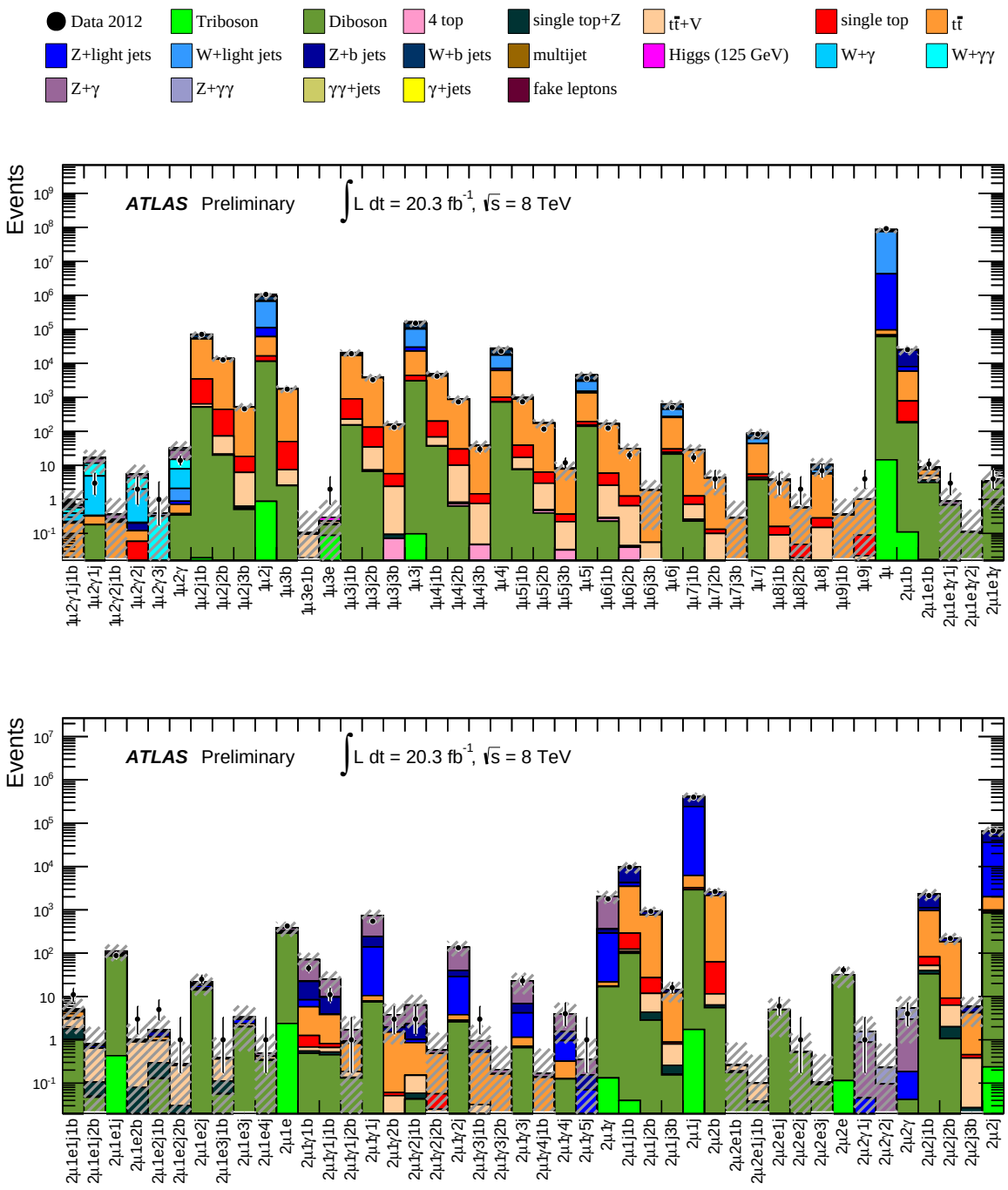

Figure 4: Number of events for event classes for which muon triggers are used. The classes are labeled according to the abundance and type (e, μ, γ, j, b, ν) of the reconstructed objects for this event class. The data are compared to the SM background expectation as described in the text. The hatched bands indicate the total uncertainty of the SM prediction.

.

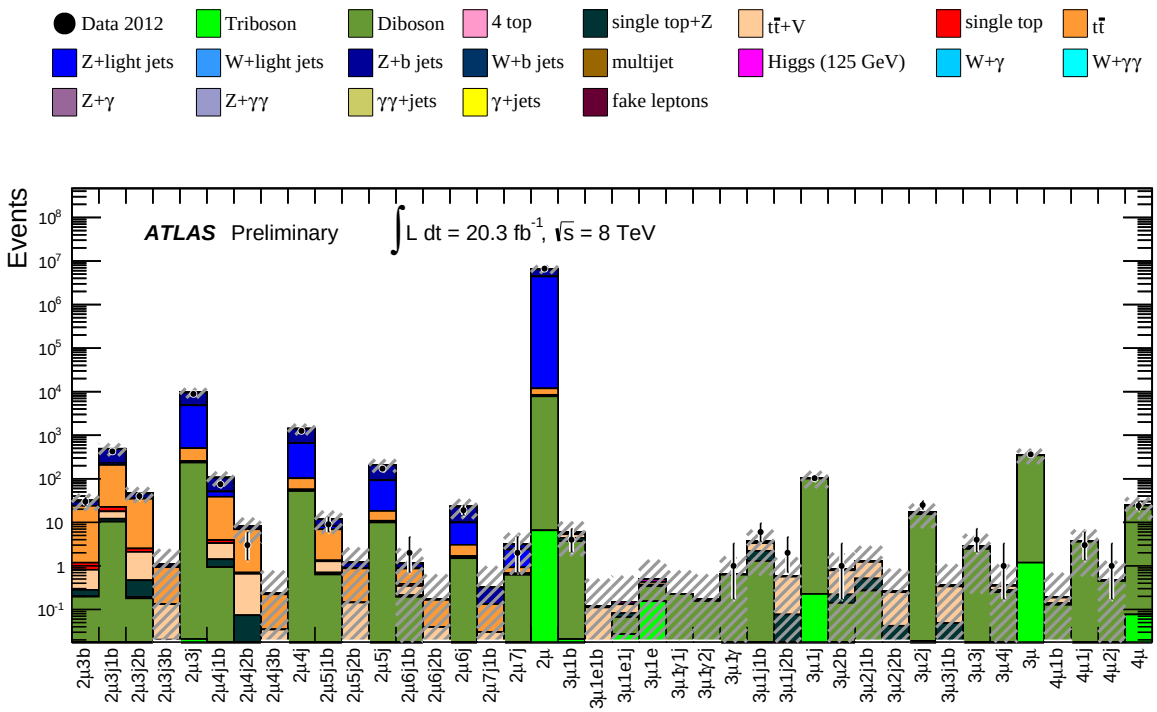

Figure 5: Number of events for event classes for which muon triggers are used. The classes are labeled according to the abundance and type (e, μ, γ, j, b, ν) of the reconstructed objects for this event class. The data are compared to the SM background expectation as described in the text. The hatched bands indicate the total uncertainty of the SM prediction.

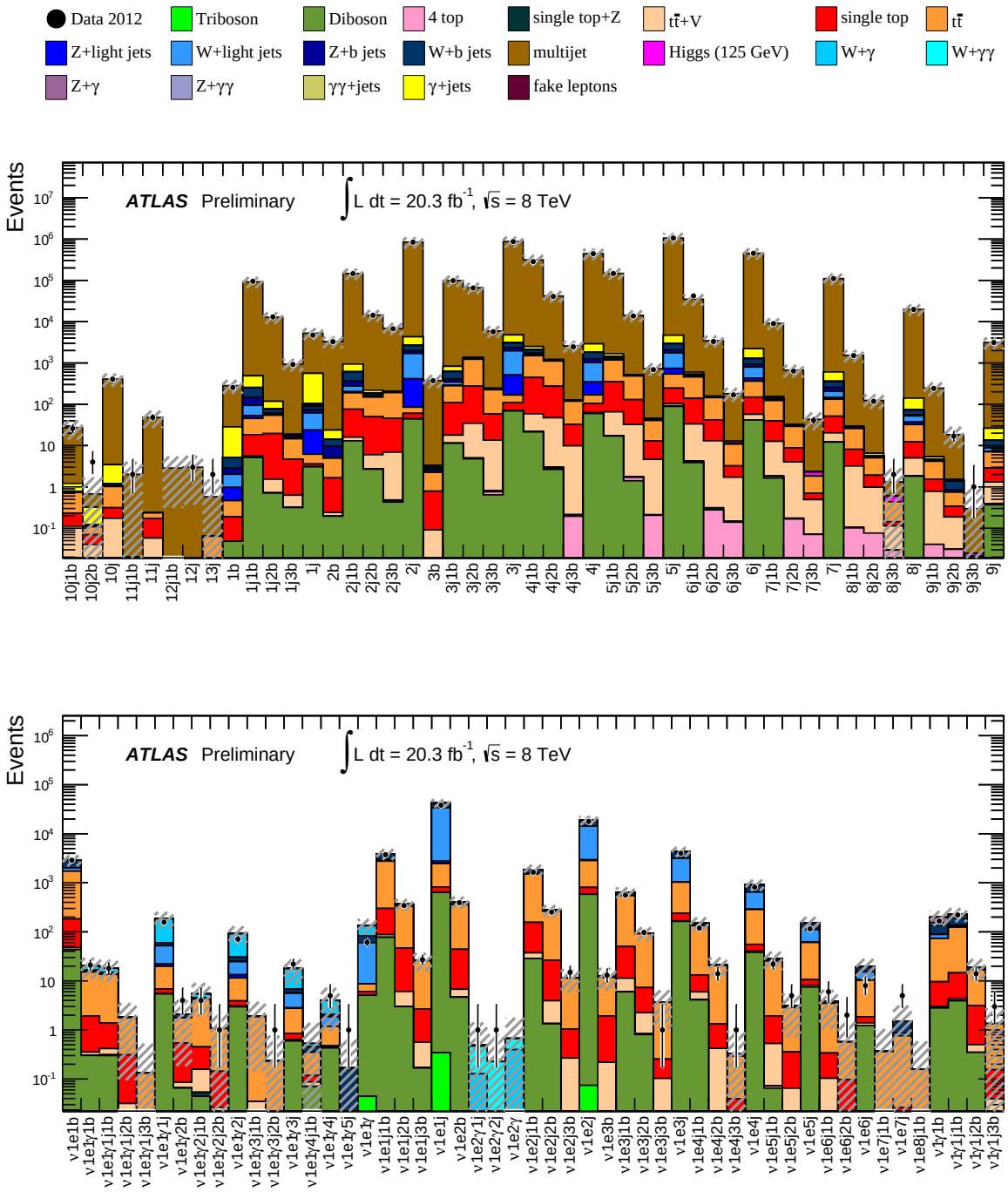

Figure 6: Number of events for event classes for which jets or $E_{\mathrm{T}}^{\mathrm{miss}}$ triggers are used. The classes are labeled according to the abundance and type (e, μ, γ, j, b, ν) of the reconstructed objects for this event class. The data are compared to the SM background expectation as described in the text. The hatched bands indicate the total uncertainty of the SM prediction.

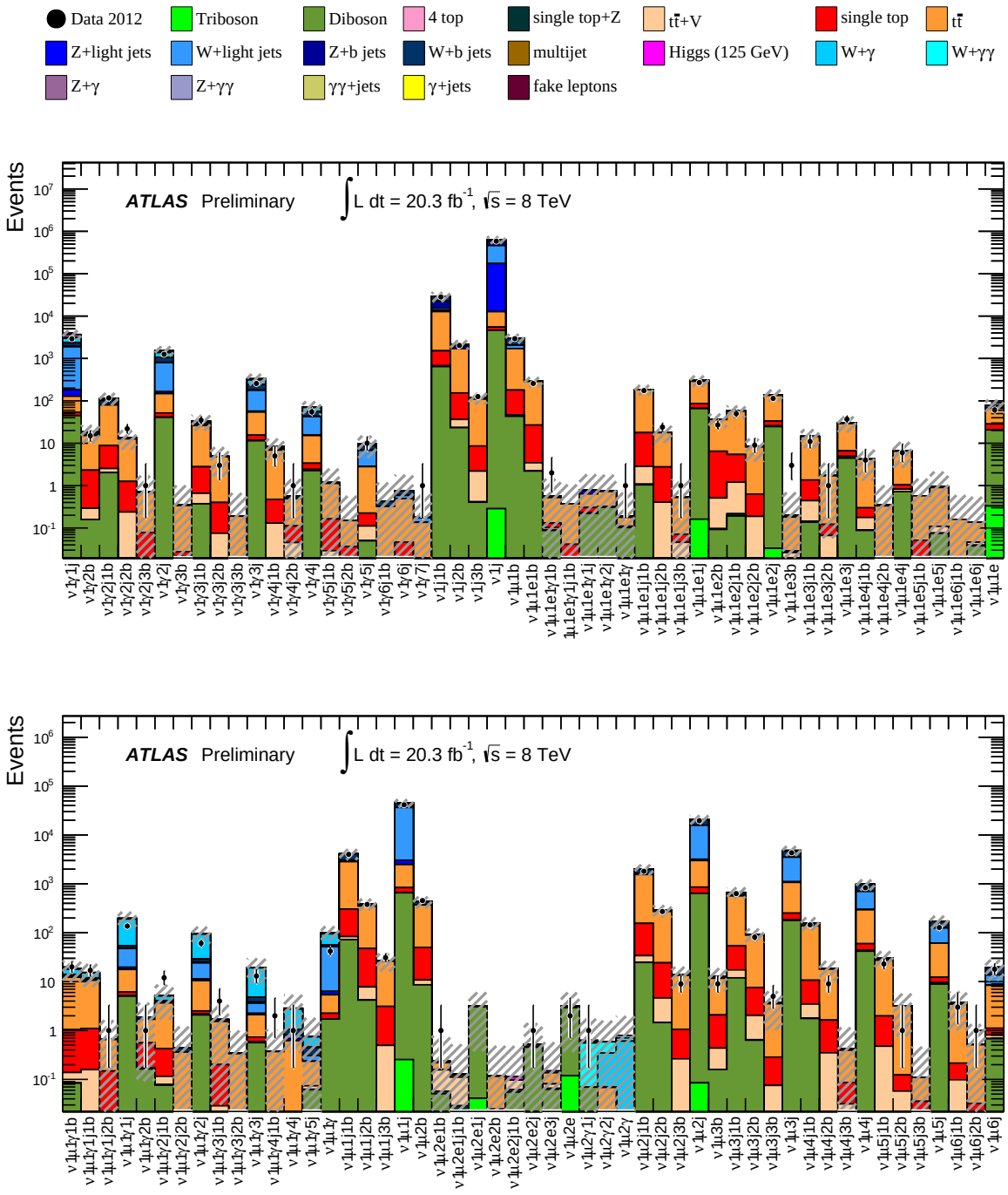

Figure 7: Number of events for event classes for which jets or $E_{\mathrm{T}}^{\mathrm{miss}}$ triggers are used. The classes are labeled according to the abundance and type (e, μ, γ, j, b, ν) of the reconstructed objects for this event class. The data are compared to the SM background expectation as described in the text. The hatched bands indicate the total uncertainty of the SM prediction.

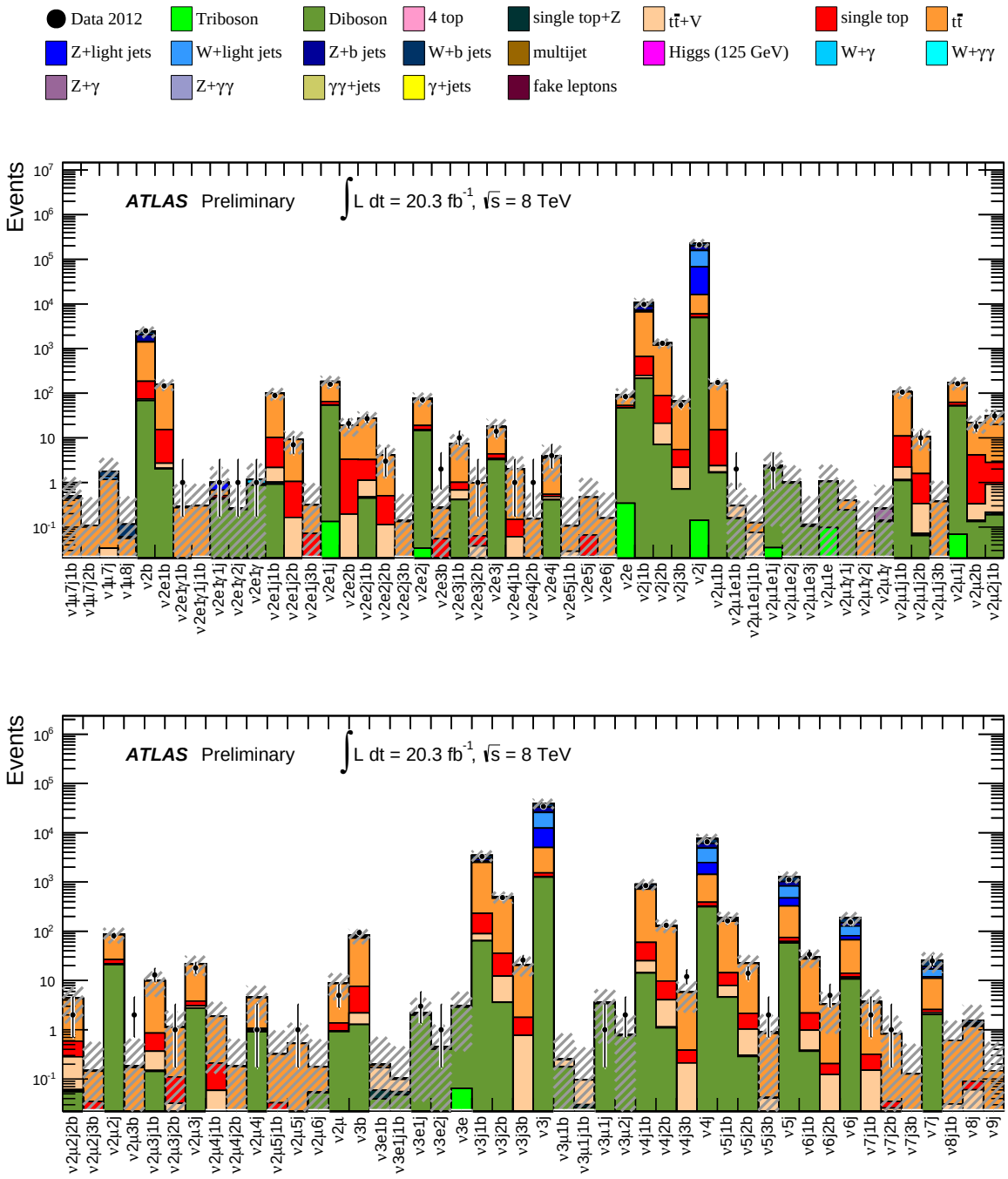

Figure 8: Number of events for event classes for which jets or $E_{\mathrm{T}}^{\mathrm{miss}}$ triggers are used. The classes are labeled according to the abundance and type (e, μ, γ, j, b, ν) of the reconstructed objects for this event class. The data are compared to the SM background expectation as described in the text. The hatched bands indicate the total uncertainty of the SM prediction.

class of new physics signals. The $m_{\rm eff}$ scan is applied to all 697 event classes with at least 0.1 expected events, while event classes with a single object have been removed from the scan of $m_{\rm inv}$. The $E_{\rm T}^{\rm miss}$ scan is applied only to categories containing ν (250 in total).

The search algorithm locates the region of largest deviation in a distribution of any shape. The bin size of the scanned distributions is chosen to reflect the expected resolution of each variable in a given class, with values ranging from 20 to 500 GeV.

In the scan of the $m_{\rm inv}$ distribution for each event class, only the region where $m_{\rm inv}$ is greater than the sum of the minimum $p_{\rm T}$ requirement of each contributing object is considered (e.g. 50 GeV for a 2μ class). This avoids sensitivity to the threshold regions which may not be well-modeled by the MC simulation.

In every histogram the number of data events $N_{\rm obs}$ and the expectation $N_{\rm SM}$ with its total systematic uncertainty $\delta N_{\rm SM}$ (obtained by summing linearly the absolute value of the uncertainty of each bin) are determined for each possible connected bin region made with a minimum of two bins. A statistical estimator p is used to judge which region is of most interest. It is derived from the convolution of a Poisson probability density function (pdf), to account for statistical uncertainties, with a Gaussian pdf, $G(b; N_{\rm SM}, \delta N_{\rm SM})$, with mean $N_{\rm SM}$ and width $\delta N_{\rm SM}$, to include systematic uncertainties. It is defined as:

$$p = \begin{cases} A \int_0^\infty db\, G(b; N_{\rm SM}, \delta N_{\rm SM}) \sum_{i=N_{\rm obs}}^{\infty} \frac{e^{-b} b^i}{i!} & \text{if } N_{\rm obs} \geq N_{\rm SM} \\ A \int_0^\infty db\, G(b; N_{\rm SM}, \delta N_{\rm SM}) \sum_{i=0}^{N_{\rm obs}} \frac{e^{-b} b^i}{i!} & \text{if } N_{\rm obs} < N_{\rm SM}. \end{cases}$$

The factor $A = 1/\int_0^\infty db\, G(b; N_{\rm SM}, \delta N_{\rm SM}) \sum_{i=0}^{\infty} \frac{e^{-b} b^i}{i!}$ ensures that the pdf is normalized to unity. If the Gaussian pdf G is replaced by a Dirac delta function $\delta(b - N_{\rm SM})$ the estimator p results in a Poisson probability. The value of p gives an estimate of the probability that the SM expectation fluctuates upwards or downwards with respect to the data in a given region. Here p is interpreted as the local p-value of this deviation. The region of greatest deviation found by the algorithm corresponds to the region with the smallest p-value. Such a method is able to find narrow resonances and single outstanding events as well as signals spread over large regions of phase space in distributions of any shape.

To avoid being sensitive to the effect of poor MC statistics, regions where the total background prediction has an uncertainty greater than 100% are discarded by the algorithm. If all regions in an event class have an uncertainty larger than 100% no region is selected, and a p-value of 1 is assigned to the class. Following this procedure we find 63 such event classes for the scan of $m_{\rm eff}$, 76 for the $m_{\rm inv}$ scan and 42 for the $E_{\rm T}^{\rm miss}$scan.

6.3 Search Results

To illustrate how the algorithm works three example distributions are presented. Figure 9 shows the effective mass distribution for the event class with two electrons, one jet and $E_{\rm T}^{\rm miss}$; Figure 10 the invariant mass for the event class with with three muons; Figure 11 shows the $E_{\rm T}^{\rm miss}$ distribution for the class containing 2 jets, 2 b-jets and $E_{\rm T}^{\rm miss}$. The region of greatest deviation found by the search algorithm in these distributions is indicated with vertical lines.

The probability that a statistical fluctuation occurs somewhere in the event class distributions is modelled by pseudo-experiments. In this procedure, the data are replaced by pseudo-data which are generated according to the SM expectation.

We generated 2000 "pseudo ATLAS experiments", each consisting of the same event classes and distributions as considered in the data. The search algorithm is applied to each of these in the same way as for data. The p-value distributions of the "pseudo ATLAS experiment" and their statistical properties

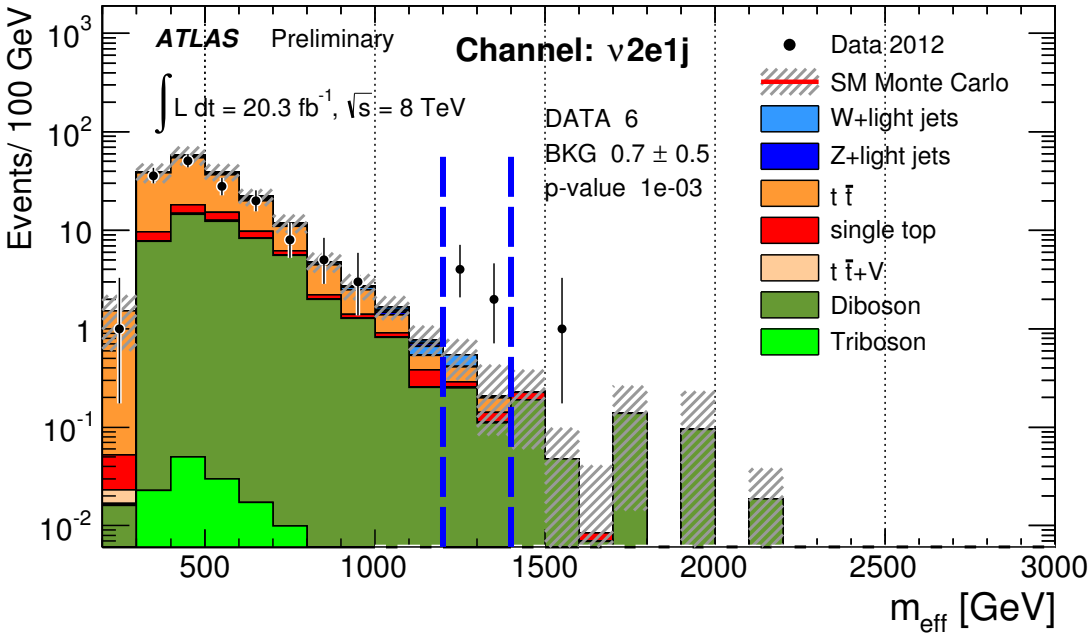

Figure 9: m_{eff} distribution for the event class with two electrons, one jet and $E_{\text{T}}^{\text{miss}}$ ($\nu 2e1j$). The dashed vertical lines indicate the region of interest which has the smallest p-value (0.0013) for this event class.

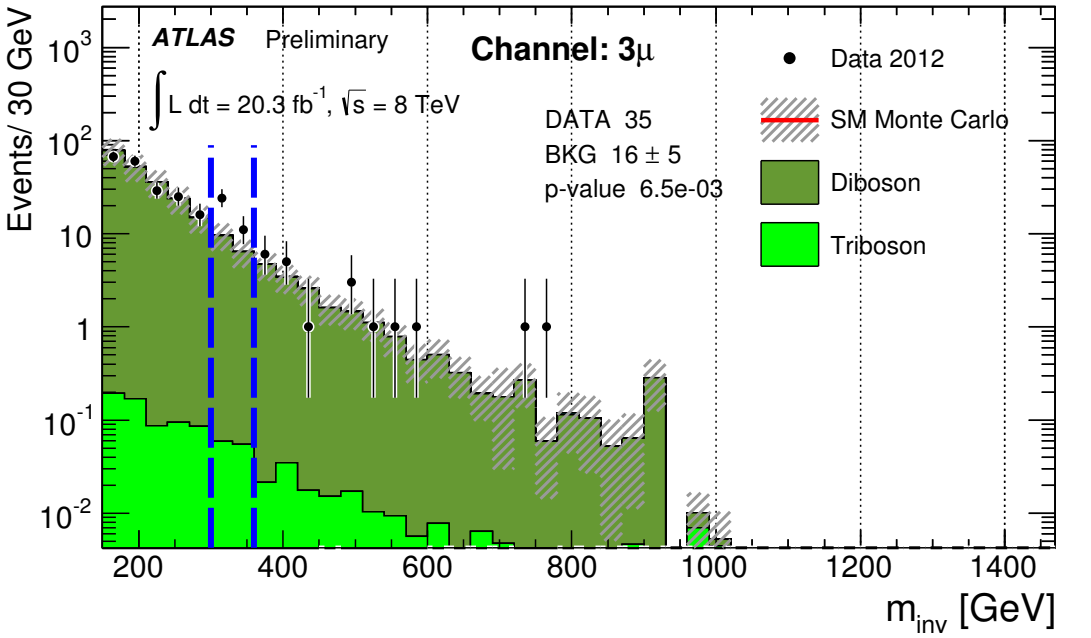

Figure 10: m_{inv} distribution for the event class with three muons (3μ). The dashed vertical lines indicate the region of interest which has the smallest p-value (0.0071) for this event class.

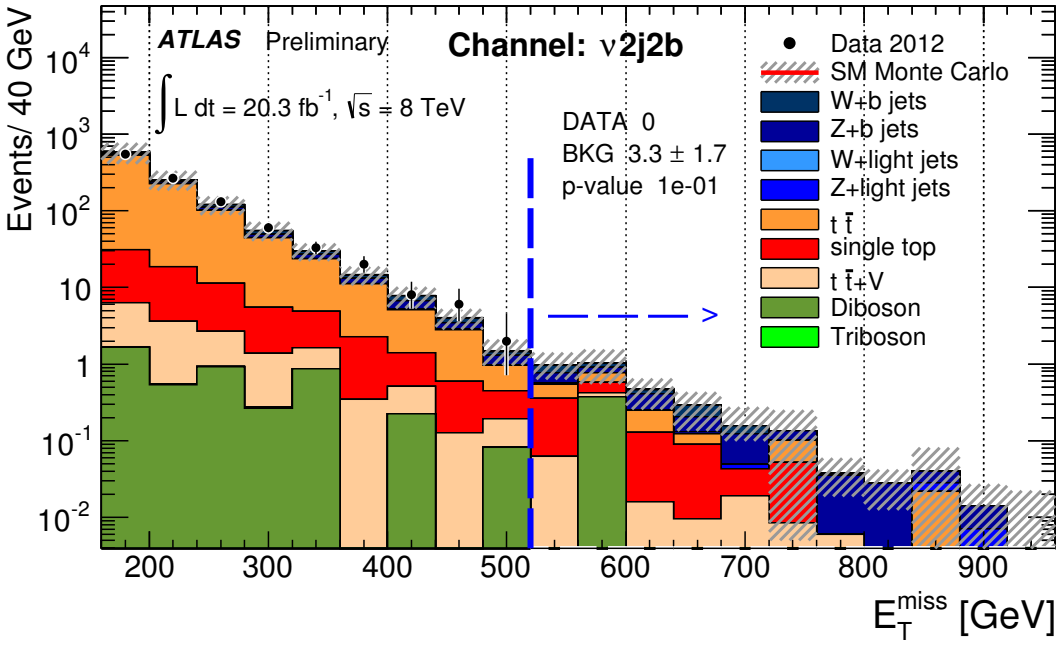

Figure 11: E_T^{miss} distribution for the event class with 2 jets, 2 b-jets and $E_{\text{T}}^{\text{miss}}$ ($\nu 2j2b$). The dashed vertical line and the arrow indicate the region of interest which has the smallest p-value (0.097) for this event class.

can be compared with the p-value distributions obtained from data. The effect of bin-by-bin correlations is taken into account in the generation of pseudo-experiments.

The distribution of the local p-values observed in data for each event class, compared to the expectation from the SM hypothesis as obtained from the pseudo-experiments, are shown in Figures 12, 14 and 16 for the m_{inv}, m_{eff} and $E_{\text{T}}^{\text{miss}}$ distributions, respectively. These figures also show for comparison the expected p-value distributions obtained when neglecting correlations in the pseudo-experiment generation. This treatment leads to smaller p-values. The probability that a single deviation occurs at very low p-values is less affected. Agreement is observed between data and the expectation from correlated systematics.

In Figures 13, 15 and 17 we show the fraction of pseudo-experiments that have at least one, two, or three deviations below a given p-value (p_{min}).

No event class is found with a local p-value below 10^{-4}, corresponding roughly to a 4 σ deviation. This is consistent with the expectation from pseudo-experiments. At least one class with a local p-value below 10^{-4} is expected to be found in less than 10% of the pseudo-experiments in the invariant mass distributions, in about 10% of the pseudo-experiments in the scan of the effective mass distributions and about 5% of the pseudo-experiments in the scan of the $E_{\text{T}}^{\text{miss}}$ distributions. One event class is found in the effective mass distribution with a p-value smaller than 10^{-3}, corresponding to a probability of about 60%. The smallest p-value obtained from the scan of the $E_{\text{T}}^{\text{miss}}$ distribution is 0.013. Pseudo-experiments would predict a slightly larger number of excesses indicating a possible overestimation of the systematic uncertainties.

The largest deviation has a local p-value of $7 \cdot 10^{-4}$ and is found in the effective mass distribution of a class with one electron, one muon, one photon and two jets.

Extensive checks have been carried out to understand how the p-value distribution changes when

using different MC generators for the main backgrounds and varying the size of the theoretical uncertainties up and down by a factor of two. The effect of these variations is found to be insignificant on the tail of the p-value distribution and on the largest deviations found.

6.4 Sensitivity to benchmark new physics signals

A set of pseudo-data samples were generated to assess the sensitivity of the search procedure to some specific signals of new physics. The prediction of a new physics model is added on top of the SM prediction and the sum is used to generate pseudo-data samples. To quantify our sensitivity we compute the fraction of pseudo-experiments in which at least one event class is expected to have a significance greater than a given value, both under the SM-only hypothesis and under the SM+signal hypothesis.

In Figure 18 (top) the effect of a signal is shown for direct stop production in the $E_{\mathrm{T}}^{\mathrm{miss}}$ scan. No significant deviation in the p-values with respect to the SM-only hypothesis is observed, due to the relatively small stop production cross-section.

In Figure 18 (middle) the effect of a signal is shown for gluino pair production in the m_{eff} scan. Pseudo-experiments for a 800 GeV gluino predict in about 95% of the cases a deviation with a p-value as low as 10^{-6}, with a probability close to zero for this to happen under the SM-only hypothesis. Due to the smaller production cross-section a gluino with a mass of 1000 GeV has a much smaller probability to yield an event class with such low p-values. Very little difference with respect to the SM expectation is visible for a gluino with a mass of 1200 GeV.

The sensitivity to the Z' signal is shown in Figure 18 (bottom). Because this signal is localized in few specific classes ($2e$, 2μ) in a narrow range of the m_{inv} distribution with low SM background the search algorithm is sensitive to it.

7 Conclusion

The data collected with the ATLAS experiment during the year 2012 in pp collisions at $\sqrt{s} = 8$ TeV, corresponding to an integrated luminosity of 20.3 fb^{-1}, have been used to search for deviations from the SM prediction at high p_{T} with a model independent approach. Event topologies involving isolated electrons, muons, photons, jets, b-jets and $E_{\mathrm{T}}^{\mathrm{miss}}$ have been systematically classified. All event classes have been scanned looking for deviations from the SM prediction in the effective mass, the visible invariant mass and the missing transverse momentum distributions. No significant excess above the SM prediction has been observed.

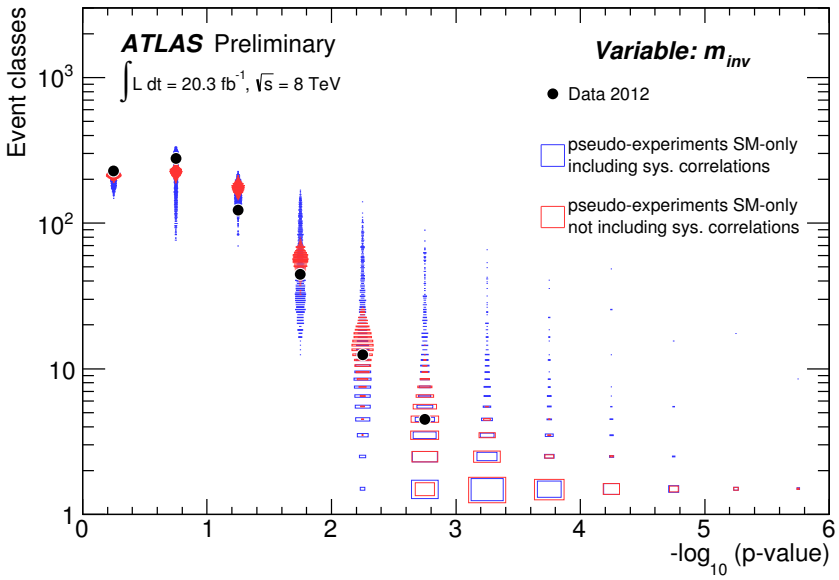

Figure 12: The observed and expected distributions for the number of event classes having a given range in $-\log_{10}$(p-value) for the scans of the visible invariant mass distributions. The data and mean expectation are shown together with the expected distributions obtained from the pseudo-experiments generated under the default assumptions for the correlations in the systematic uncertainties (blue) and neglecting their correlations (red).

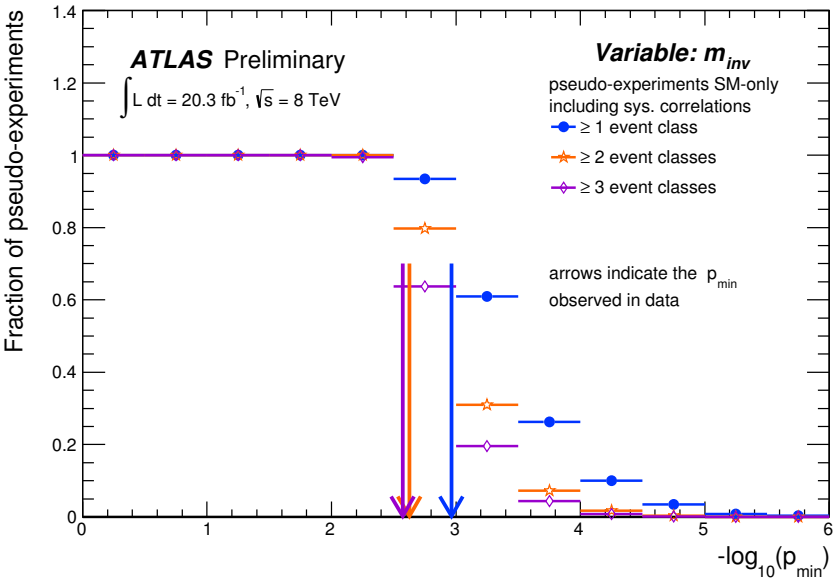

Figure 13: The fraction of pseudo-experiments which have at least one, two and three deviations with a p-value below a given threshold (p_{min}) in the scan of the visible invariant mass distribution. The values observed in data are indicated by arrows. Pseudo-experiments are generated under the SM-only hypothesis and with the default assumption for the correlations in the systematic uncertainties.

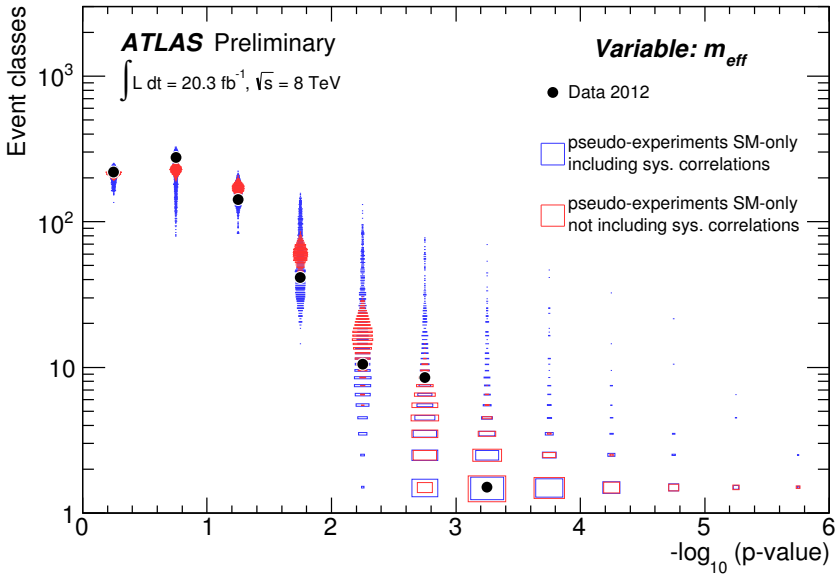

Figure 14: The observed and expected distributions for the number of event classes having a given range in $-\log_{10}$(p-value) for the scans of the effective mass distributions. The data and mean expectation are shown together with the expected distributions obtained from the pseudo-experiments generated under the default assumptions for the correlations in the systematic uncertainties (blue) and neglecting their correlations (red).

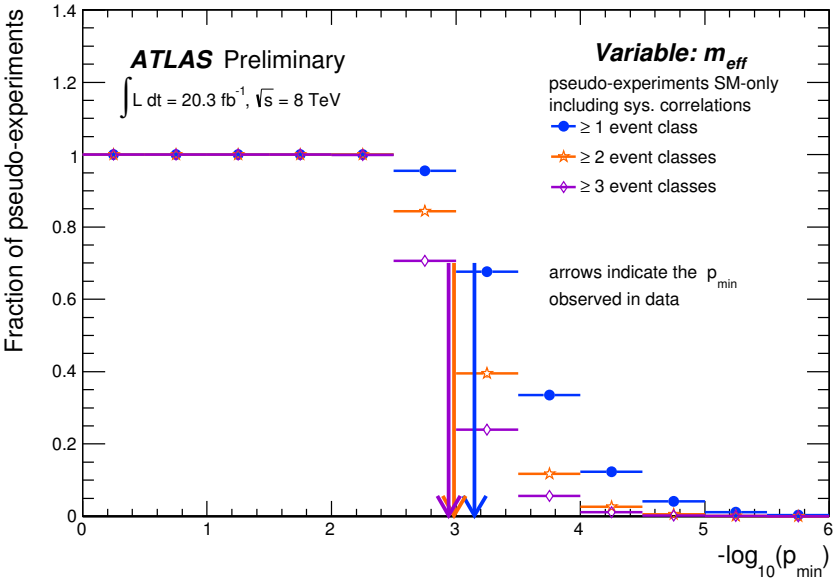

Figure 15: The fraction of pseudo-experiments which have at least one, two and three deviations with a p-value below a given threshold (p_{min}) in the scan of the effective mass distribution. The values observed in data are indiccated by arrows. Pseudo-experiments are generated under the SM-only hypothesis and with the default assumption for the correlations in the systematic uncertainties.

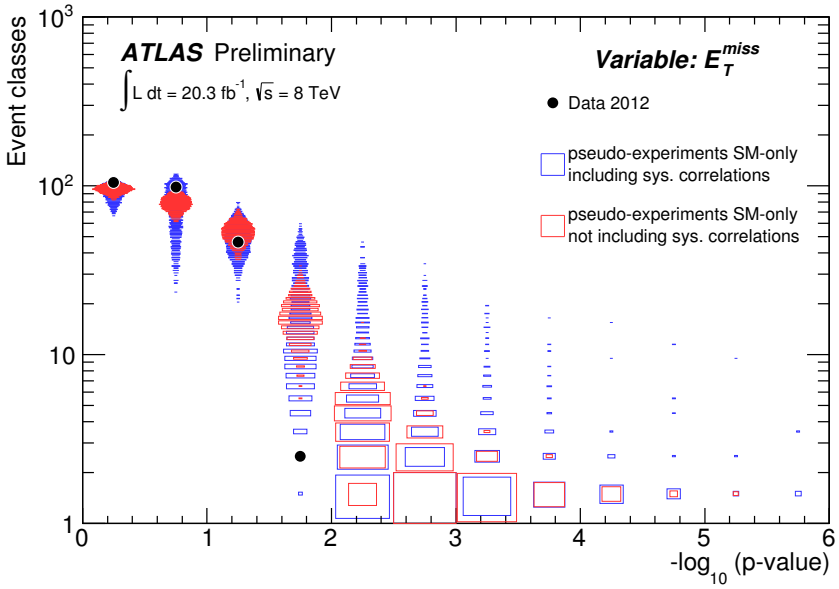

Figure 16: The observed and expected distributions for the number of event classes having a given range in $-\log_{10}$(p-value) for the scans of the missing transverse energy distributions. The data and mean expectation are shown together with the expected distributions obtained from the pseudo-experiments generated under the default assumptions for the correlations in the systematic uncertainties (blue) and neglecting their correlations (red).

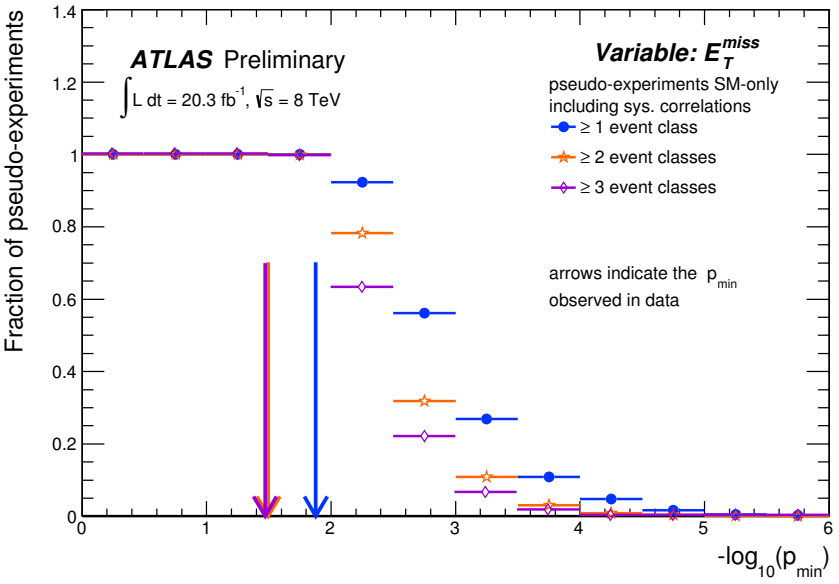

Figure 17: The fraction of pseudo-experiments which have at least one, two and three deviations with a p-value below a given threshold (p_{min}) in the scan of the missing transverse energy distribution. The values observed in data are indicated by arrows. Pseudo-experiments are generated under the SM-only hypothesis and with the default assumption for the correlations in the systematic uncertainties.

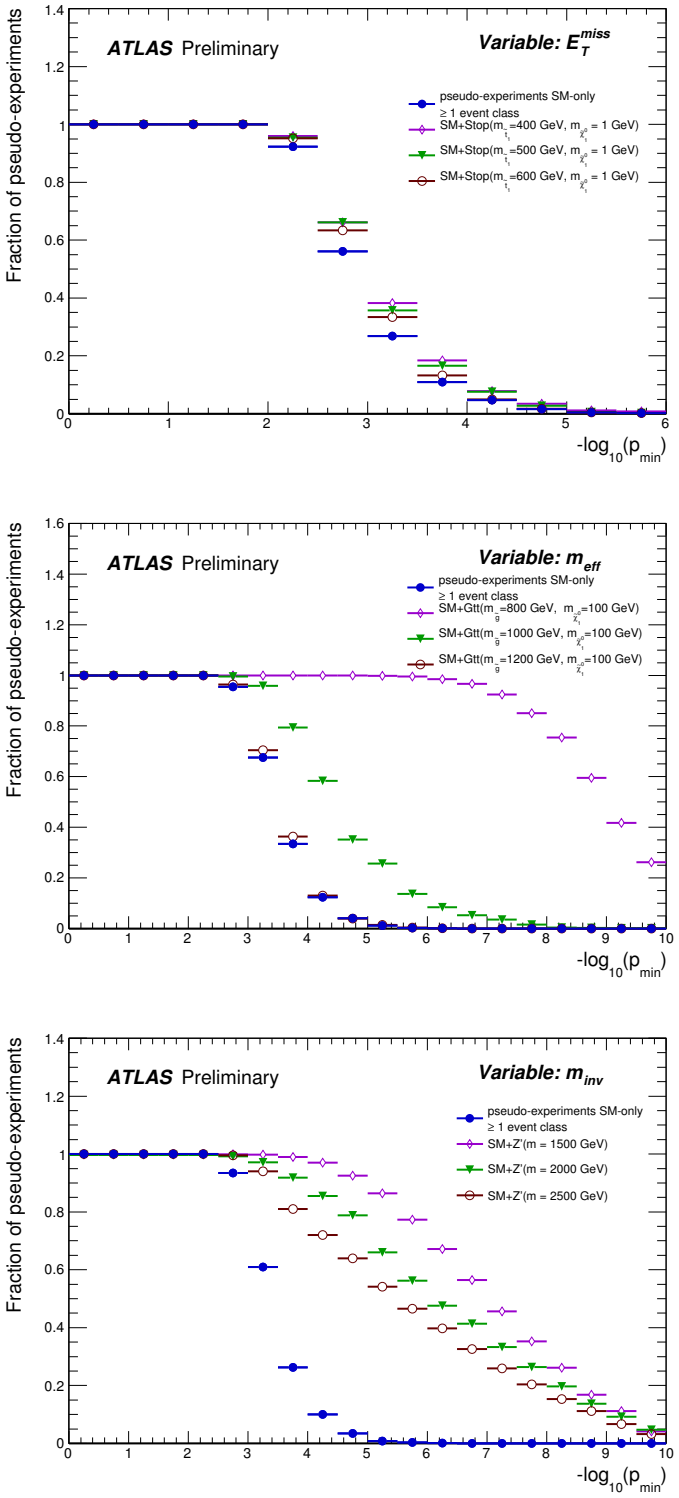

Figure 18: Sensitivity of the search method to benchmark signal models. The figure shows the expected fraction of pseudo-experiments having at least one event class with a $-\log_{10}$(p-value) greater than the one shown on the axis for pseudo-experiments generated under the SM-only and SM+signal hypothesis. The top figure shows a model of direct stop production for the scan of the $E_{\mathrm{T}}^{\mathrm{miss}}$ distribution. The middle figure shows the fraction of pseudo-experiments for the production of a gluino pair with various gluino masses considering the m_{eff} scans. The lower figure shows the fraction of pseudo-experiments for Z' signal considering the m_{inv} scans.

References

[1] ATLAS Collaboration, *A general search for new phenomena with the ATLAS detector in pp collisions at* $\sqrt{s}$ = 7 *TeV*, ATLAS-COM-CONF-2012-107.

[2] D0 Collaboration, B. Abbott et al., *Search for new physics in eμX data at DØ using SLEUTH: A quasi-model-independent search strategy for new physics*, Phys. Rev. D **62** (2000) 092004.

[3] H1 Collaboration, A. Aktas et al., *A general search for new phenomena in ep scattering at HERA*, Phys.Lett. **B602** (2004) 14–30, arXiv:hep-ex/0408044 [hep-ex].

[4] H1 Collaboration, F. Aaron et al., *A General Search for New Phenomena at HERA*, Phys.Lett. **B674** (2009) 257–268, arXiv:0901.0507 [hep-ex].

[5] CDF Collaboration, T. Aaltonen, et al., *Model-independent and quasi-model-independent search for new physics at CDF*, Phys. Rev. D **78** (2008) 012002, arXiv:0712.1311 [hep-ex].

[6] CMS Collaboration, *Model Unspecific Search for New Physics in pp Collisions at sqrt(s) = 7 TeV*, CMS-PAS-EXO-10-021.

[7] ATLAS Collaboration, *The ATLAS Experiment at the CERN Large Hadron Collider*, JINST **3** (2008) S08003.

[8] GEANT4 Collaboration, S. Agostinelli et al., *GEANT4: A simulation toolkit*, Nucl. Instrum. Meth. **A506** (2003) 250–303.

[9] ATLAS Collaboration, *The ATLAS Simulation Infrastructure*, Eur. Phys. J. **C70** (2010) 823–874, arXiv:1005.4568 [physics.ins-det].

[10] ATLAS Collaboration, *The simulation principle and performance of the ATLAS fast calorimeter simulation FastCaloSim*, ATL-PHYS-PUB-2010-013.

[11] T. Sjostrand, S. Mrenna, and P. Z. Skands, *A Brief Introduction to PYTHIA 8.1*, Comput. Phys. Commun. **178** (2008) 852–867, arXiv:0710.3820.

[12] ATLAS Collaboration, *Further ATLAS tunes of PYTHIA 6 and Pythia 8*, ATL-PHYS-PUB-2011-014.

[13] A. Martin, W. Stirling, R. Thorne, and G. Watt, *Parton distributions for the LHC*, Eur.Phys.J. **C63** (2009) 189–285, arXiv:0901.0002 [hep-ph].

[14] T. Gleisberg, S. Hoeche, F. Krauss, M. Schonherr, S. Schumann, et al., *Event generation with SHERPA 1.1*, JHEP **0902** (2009) 007, arXiv:0811.4622 [hep-ph].

[15] K. Melnikov and F. Petriello, *Electroweak gauge boson production at hadron colliders through O(alpha(s)**2)*, Phys. Rev. **D74** (2006) 114017, arXiv:hep-ph/0609070.

[16] H.-L. Lai et al., *New parton distributions for collider physics*, Phys. Rev. **D82** (2010) 074024, arXiv:1007.2241 [hep-ph].

[17] T. Sjostrand, S. Mrenna, and P. Z. Skands, *PYTHIA 6.4 Physics and Manual*, JHEP **0605** (2006) 026, arXiv:hep-ph/0603175.

[18] M. L. Mangano et al., *ALPGEN, a generator for hard multiparton processes in hadronic collisions*, JHEP **07** (2003) 001, arXiv:hep-ph/0206293.

[19] P. M. Nadolsky et al., *Implications of CTEQ global analysis for collider observables*, Phys. Rev. **D78** (2008) 013004.

[20] G. Bozzi, F. Campanario, M. Rauch, and D. Zeppenfeld, *$Z\gamma\gamma$ production with leptonic decays and triple photon production at NLO QCD*, Phys.Rev. **D84** (2011) 074028, arXiv:1107.3149 [hep-ph].

[21] G. Bozzi, F. Campanario, M. Rauch, and D. Zeppenfeld, *$W^{+-}\gamma\gamma$ production with leptonic decays at NLO QCD*, Phys.Rev. **D83** (2011) 114035, arXiv:1103.4613 [hep-ph].

[22] S. Alioli, P. Nason, C. Oleari, and E. Re, *A general framework for implementing NLO calculations in shower Monte Carlo programs: the POWHEG BOX*, JHEP **1006** (2010) 043, arXiv:1002.2581 [hep-ph].

[23] M. Cacciari, M. Czakon, M. Mangano, A. Mitov, and P. Nason, *Top-pair production at hadron colliders with next-to-next-to-leading logarithmic soft-gluon resummation*, Phys.Lett. **B710** (2012) 612–622, arXiv:1111.5869 [hep-ph].

[24] P. Baernreuther, M. Czakon, and A. Mitov, *Percent Level Precision Physics at the Tevatron: First Genuine NNLO QCD Corrections to $q\bar{q} \to t\bar{t} + X$*, Phys.Rev.Lett. **109** (2012) 132001, arXiv:1204.5201 [hep-ph].

[25] M. Czakon and A. Mitov, *NNLO corrections to top pair production at hadron colliders: the quark-gluon reaction*, JHEP **1301** (2013) 080, arXiv:1210.6832 [hep-ph].

[26] M. Czakon and A. Mitov, *NNLO corrections to top-pair production at hadron colliders: the all-fermionic scattering channels*, JHEP **1212** (2012) 054, arXiv:1207.0236 [hep-ph].

[27] M. Czakon, P. Fiedler, and A. Mitov, *The total top quark pair production cross-section at hadron colliders through $O(\alpha_s^4)$*, Phys.Rev.Lett. **110** (2013) 252004, arXiv:1303.6254 [hep-ph].

[28] M. Czakon and A. Mitov, *Top++: A Program for the Calculation of the Top-Pair Cross-Section at Hadron Colliders*, arXiv:1112.5675 [hep-ph].

[29] N. Kidonakis, *Next-to-next-to-leading-order collinear and soft gluon corrections for t-channel single top quark production*, Phys.Rev. **D83** (2011) 091503, arXiv:1103.2792 [hep-ph].

[30] N. Kidonakis, *Two-loop soft anomalous dimensions for single top quark associated production with a W- or H-*, Phys.Rev. **D82** (2010) 054018, arXiv:1005.4451 [hep-ph].

[31] N. Kidonakis, *NNLL resummation for s-channel single top quark production*, Phys.Rev. **D81** (2010) 054028, arXiv:1001.5034 [hep-ph].

[32] J. M. Campbell and R. K. Ellis, *$t\bar{t}W$ production and decay at NLO*, JHEP **1207** (2012) 052, arXiv:1204.5678 [hep-ph].

[33] M. Garzelli, A. Kardos, C. Papadopoulos, and Z. Trocsanyi, *$t\,\bar{t}\,W^{+-}$ and $t\,\bar{t}\,Z$ Hadroproduction at NLO accuracy in QCD with Parton Shower and Hadronization effects*, JHEP **1211** (2012) 056, arXiv:1208.2665 [hep-ph].

[34] J. M. Campbell, R. K. Ellis, and C. Williams, *Vector boson pair production at the LHC*, JHEP **1107** (2011) 018, arXiv:1105.0020 [hep-ph].

[35] F. Campanario, V. Hankele, C. Oleari, S. Prestel, and D. Zeppenfeld, *QCD corrections to charged triple vector boson production with leptonic decay*, Phys.Rev. **D78** (2008) 094012, arXiv:0809.0790 [hep-ph].

[36] https://twiki.cern.ch/twiki/bin/view/LHCPhysics/CERNYellowReportPageAt8TeV.

[37] H. Miyazawa, *Baryon Number Changing Currents*, Prog. Theor. Phys. **36 (6)** (1966) 1266–1276.

[38] P. Ramond, *Dual Theory for Free Fermions*, Phys. Rev. **D3** (1971) 2415–2418.

[39] Y. Golfand and E. Likhtman, *Extension of the Algebra of Poincare Group Generators and Violation of p Invariance*, JETP Lett. **13** (1971) 323–326.

[40] A. Neveu and J. Schwarz, *Factorizable dual model of pions*, Nucl. Phys. **B31** (1971) 86–112.

[41] A. Neveu and J. Schwarz, *Quark Model of Dual Pions*, Phys. Rev. **D4** (1971) 1109–1111.

[42] J. Gervais and B. Sakita, *Field theory interpretation of supergauges in dual models*, Nucl. Phys. **B34** (1971) 632–639.

[43] D. Volkov and V. Akulov, *Is the Neutrino a Goldstone Particle?*, Phys. Lett. **B46** (1973) 109–110.

[44] J. Wess and B. Zumino, *A Lagrangian Model Invariant Under Supergauge Transformations*, Phys. Lett. **B49** (1974) 52.

[45] J. Wess and B. Zumino, *Supergauge Transformations in Four-Dimensions*, Nucl. Phys. **B70** (1974) 39–50.

[46] M. Bahr et al., *Herwig++ Physics and Manual*, Eur. Phys. J. **C58** (2008) 639–707, arXiv:0803.0883 [hep-ph].

[47] W. Beenakker, R. Hopker, M. Spira, and P. M. Zerwas, *Squark and gluino production at hadron colliders*, Nucl. Phys. **B492** (1997) 51–103, arXiv:hep-ph/9610490.

[48] A. Kulesza and L. Motyka, *Threshold resummation for squark-antisquark and gluino-pair production at the LHC*, Phys.Rev.Lett. **102** (2009) 111802, arXiv:0807.2405 [hep-ph].

[49] A. Kulesza and L. Motyka, *Soft gluon resummation for the production of gluino-gluino and squark-antisquark pairs at the LHC*, Phys.Rev. **D80** (2009) 095004, arXiv:0905.4749 [hep-ph].

[50] W. Beenakker, S. Brensing, M. Kramer, A. Kulesza, E. Laenen, et al., *Soft-gluon resummation for squark and gluino hadroproduction*, JHEP **0912** (2009) 041, arXiv:0909.4418 [hep-ph].

[51] W. Beenakker, S. Brensing, M. Kramer, A. Kulesza, E. Laenen, et al., *Squark and gluino hadroproduction*, Int.J.Mod.Phys. **A26** (2011) 2637–2664, arXiv:1105.1110 [hep-ph].

[52] P. Langacker, *The Physics of Heavy Z' Gauge Bosons*, Rev.Mod.Phys. **81** (2009) 1199–1228, arXiv:0801.1345 [hep-ph].

[53] M. Cacciari, G. P. Salam, and G. Soyez, *The anti-k_t jet clustering algorithm*, JHEP **04** (2008) 063, arXiv:0802.1189 [hep-ph].

[54] M. Cacciari and G. P. Salam, *Dispelling the N^3 myth for the k_t jet-finder*, Phys. Lett. **B641** (2006) 57–61, arXiv:hep-ph/0512210.

[55] ATLAS Collaboration, *Jet energy measurement with the ATLAS detector in proton-proton collisions at* $\sqrt{s} = 7$ *TeV*, Eur.Phys.J. **C73** (2013) 2304, arXiv:1112.6426 [hep-ex].

[56] W. Lampl et al., *Calorimeter Clustering Algorithms: Description and Performance*, ATL-LARG-PUB-2008-002.

[57] ATLAS Collaboration, *Jet energy scale and its systematic uncertainty in proton-proton collisions at* $\sqrt{s} = 7$ *TeV in ATLAS 2010 data*, ATLAS-CONF-2011-032.

[58] M. Cacciari and G. P. Salam, *Pileup subtraction using jet areas*, Phys.Lett. **B659** (2008) 119–126, arXiv:0707.1378 [hep-ph].

[59] ATLAS Collaboration, *Pile-up subtraction and suppression for jets in ATLAS*, ATLAS-CONF-2013-083.

[60] ATLAS Collaboration, *Commissioning of the ATLAS high-performance b-tagging algorithms in the 7 TeV collision data*, ATLAS-CONF-2011-102.

[61] ATLAS Collaboration, *Measuring the b-tag efficiency in a top-pair sample with 4.7* fb^{-1} *of data from the ATLAS detector*, ATLAS-CONF-2012-097.

[62] ATLAS Collaboration, *Electron performance measurements with the ATLAS detector using the 2010 LHC proton-proton collision data*, Eur.Phys.J. **C72** (2012) 1909, arXiv:1110.3174 [hep-ex].

[63] ATLAS Collaboration, *Measurement of the production cross section of an isolated photon associated with jets in proton-proton collisions at* $\sqrt{s} = 7$ *TeV with the ATLAS detector*, Phys.Rev. **D85** (2012) 092014, arXiv:1203.3161 [hep-ex].

[64] ATLAS Collaboration, "Expected performance of the atlas experiment - detector, trigger and physics." CERN-OPEN-2008-020.

[65] ATLAS Collaboration, *Performance of Missing Transverse Momentum Reconstruction in Proton-Proton Collisions at 7 TeV with ATLAS*, Eur.Phys.J. **C72** (2012) 1844, arXiv:1108.5602 [hep-ex].

[66] ATLAS Collaboration, *Search for squarks and gluinos with the ATLAS detector in final states with jets and missing transverse momentum and* 20.3fb^{-1} *of* $\sqrt{s} = 8$ *TeV proton-proton collisions*, ATLAS-CONF-2013-047.

[67] ATLAS Collaboration, *Search for pair produced top squarks decaying into a charm quark and the lightest neutralinos with* 20.3fb^{-1} *of pp collisions at* $\sqrt{s} = 8$ *TeV with the ATLAS detector at the LHC*, ATLAS-CONF-2013-068.

[68] ATLAS Collaboration, *Search for squarks and gluinos in events with isolated leptons, jets and missing transverse momentum at* $\sqrt{s} = 8$ *TeV with the ATLAS detector at the LHC*, ATLAS-CONF-2013-062.

[69] ATLAS Collaboration, *Single hadron response measurement and calorimeter jet energy scale uncertainty with the ATLAS detector at the LHC*, Eur.Phys.J. **C73** (2013) 2305, arXiv:1203.1302 [hep-ex].

[70] ATLAS Collaboration, *Jet energy scale and its systematic uncertainty in proton-proton collisions at sqrt(s)=7 TeV with ATLAS 2011 data*, ATLAS-CONF-2013-004.

[71] ATLAS Collaboration, *Jet energy resolution and selection efficiency relative to track jets from in-situ techniques with the ATLAS Detector Using Proton-Proton Collisions at a Center of Mass Energy* $\sqrt{s} = 7$ *TeV*,. ATLAS-CONF-2010-054.

[72] ATLAS Collaboration, *Measurement of the b-tag Efficiency in a Sample of Jets Containing Muons with 5* fb^{-1} *of Data from the ATLAS Detector*, ATLAS-CONF-2012-043.

[73] ATLAS Collaboration, *Measurement of the Mistag Rate with 5*fb^{-1} *of Data Collected by the ATLAS Detector*, ATLAS-CONF-2012-040.

[74] ATLAS Collaboration, *Measurements of the photon identification efficiency with the ATLAS detector using 4.9* fb^{-1} *of pp collision data collected in 2011*, ATLAS-CONF-2012-123.

[75] ATLAS Collaboration, *Improved luminosity determination in pp collisions at* $\sqrt{s} = 7$ *TeV using the ATLAS detector at the LHC*, Eur.Phys.J. **C73** (2013) 2518, arXiv:1302.4393 [hep-ex].

[76] ATLAS Collaboration, *Measurement of multi-jet cross sections in proton-proton collisions at a 7 TeV center-of-mass energy*, Eur.Phys.J. **C71** (2011) 1763, arXiv:1107.2092 [hep-ex].

[77] ATLAS Collaboration, *Measurement of the production cross section for Z/gamma* in association with jets in pp collisions at* $\sqrt{s}$*= 7 TeV TeV with the ATLAS detector*, Phys.Rev. **D85** (2012) 032009, arXiv:1111.2690 [hep-ex].

[78] S. Moch and P. Uwer, *Theoretical status and prospects for top-quark pair production at hadron colliders*, Phys.Rev. **D78** (2008) 034003, arXiv:0804.1476 [hep-ph].

[79] ATLAS Collaboration, *Measurement of the WW cross section in* $\sqrt{s} = 7$ *TeV pp collisions with the ATLAS detector and limits on anomalous gauge couplings*, Phys.Lett. **B712** (2012) 289–308, arXiv:1203.6232 [hep-ex].

[80] ATLAS Collaboration, *Search for associated production of the Higgs boson in the* $WH \to WWW^{(*)} \to lvlvlv$ *and* $ZH \to ZWW^{(*)} \to lllvlv$ *channels with the ATLAS detector at the LHC*, ATLAS-CONF-2013-075.